

## CALIBRATING STAR FORMATION IN *WISE* USING TOTAL INFRARED LUMINOSITY

M.E. CLUVER,<sup>1,2</sup> T.H. JARRETT,<sup>3</sup> D.A. DALE,<sup>4</sup> J.-D.T. SMITH,<sup>5</sup> T. AUGUST,<sup>3</sup> AND M.J.I. BROWN<sup>6</sup>

<sup>1</sup>*Department of Physics and Astronomy, University of the Western Cape, Robert Sobukwe Road, Bellville, South Africa*

<sup>2</sup>*Inter-University Institute for Data Intensive Astronomy*

<sup>3</sup>*Department of Astronomy, University of Cape Town, Rondebosch, South Africa*

<sup>4</sup>*Department of Physics and Astronomy, University of Wyoming, Laramie, WY 82071, USA*

<sup>5</sup>*Ritter Astrophysical Observatory, University of Toledo, Toledo, OH 43606, USA*

<sup>6</sup>*School of Physics and Astronomy, Monash University, Clayton 3800, Victoria, Australia*

(Received 2017 August 24; Revised 2017 October 9; Accepted 2017 October 9; Published 2017 November 17)

Submitted to ApJ

### ABSTRACT

We present accurate resolved *WISE* photometry of galaxies in the combined SINGS and KINGFISH sample. The luminosities in the W3  $12\mu\text{m}$  and W4  $23\mu\text{m}$  bands are calibrated to star formation rates (SFRs) derived using the total infrared luminosity, avoiding UV/optical uncertainties due to dust extinction corrections. The W3 relation has a  $1\text{-}\sigma$  scatter of 0.15 dex over nearly 5 orders of magnitude in SFR and  $12\mu\text{m}$  luminosity, and a range in host stellar mass from dwarf ( $10^7 M_\odot$ ) to  $\sim 3 \times M_\star$  ( $10^{11.5} M_\odot$ ) galaxies. In the absence of deep silicate absorption features and powerful active galactic nuclei, we expect this to be a reliable SFR indicator chiefly due to the broad nature of the W3 band. By contrast the W4 SFR relation shows more scatter ( $1\text{-}\sigma = 0.18$  dex). Both relations show reasonable agreement with radio continuum-derived SFRs and excellent accord with so-called “hybrid”  $\text{H}\alpha + 24\mu\text{m}$  and FUV+ $24\mu\text{m}$  indicators. Moreover, the *WISE* SFR relations appear to be insensitive to the metallicity range in the sample. We also compare our results with IRAS-selected luminous infrared galaxies, showing that the *WISE* relations maintain concordance, but systematically deviate for the most extreme galaxies. Given the all-sky coverage of *WISE* and the performance of the W3 band as a SFR indicator, the  $L_{12\mu\text{m}}$  SFR relation could be of great use to studies of nearby galaxies and forthcoming large area surveys at optical and radio wavelengths.

*Keywords:* galaxies: photometry, star formation — infrared: galaxies — surveys

arXiv:1710.03469v2 [astro-ph.GA] 28 May 2018

## 1. INTRODUCTION

Mapping the build-up of stellar mass underpins galaxy evolution studies and tests of the  $\Lambda$ CDM cosmological framework that informs simulations of our Universe. Accurate star formation rates therefore form the cornerstone of extragalactic studies and have been the subject of vigorous study for at least the past three decades (see reviews by Kennicutt 1998; Calzetti 2013). However, the determination of a star formation rate (SFR) for any given galaxy is inherently difficult; active star formation is associated with copious dust, which itself obscures the radiation from the hot, young stars one is trying to measure. The ultraviolet (UV) directly traces the youngest stellar populations and therefore represents the “purest” star formation indicator. However, the UV is heavily extinguished by dust, and although numerous methods exist to correct for this dust extinction, variations in dust content and geometry unavoidably produce large scatter (e.g. Calzetti et al. 2007).

The optical nebular recombination lines are less affected by dust compared to the UV, and of these the  $H\alpha$  emission line is the least attenuated. However, uncertainties still arise due to the variation of the dust extinction from location to location and the assumption of the underlying stellar absorption (e.g. Calzetti et al. 2007).  $H\alpha$  maps, corrected for extinction, have been successfully used to trace star formation (e.g. Casasola et al. 2015) and with increased access to integral field observations, studies of the impact of aperture corrections on particularly single-fiber-derived SFRs advocate caution to avoid systematic bias (e.g. Iglesias-Páramo et al. 2013; Richards et al. 2016).

Surveys with multiwavelength coverage can rely on multiband photometry combined with spectral energy distribution (SED) models to determine the physical properties of galaxies using codes such as MAGPHYS (da Cunha et al. 2008) and CIGALE (Noll et al. 2009). However, full radiative transfer solutions (e.g. Natale et al. 2014; Grootes et al. 2017) will ultimately be crucial to disentangling star formation processes within galaxies.

Exploiting dust emission itself as a measure of the SFR, i.e. calibrating dust reprocessed starlight, has its own pitfalls (for a detailed review see Calzetti 2013). Using emission from  $\sim 5 - 1000 \mu\text{m}$ , usually termed the total infrared luminosity or  $L_{\text{TIR}}$ , has the advantage of sampling dust heated by young (1 - 100 Myr), UV-luminous O and B stars, as well as intermediate mass (2 - 3  $M_{\odot}$ ), UV-faint A and F stellar populations. However, having a well-sampled dust SED is observationally intensive and can only be achieved using space-based observatories. For example, the ongoing DustPedia project (Davies et al. 2017) leverages *Herschel Space Observa-*

*tory* (Pilbratt et al. 2010) and *Planck* (Planck Collaboration et al. 2016) observations with ancillary archival multiwavelength data to produce Bayesian SED fits and photon tracing radiative transfer modeling, providing a legacy dataset for exploring how dust emission is related to its physical properties and origins.

Hybrid SFR indicators compensate for extinction effects by combining a dust-obscured star formation tracer with an unobscured measure of star formation (see, for example, Calzetti et al. 1995; Buat et al. 1999). Seminal work by Kennicutt et al. (2007) and Calzetti et al. (2007), combining  $H\alpha$  and  $24\mu\text{m}$ , was expanded by Kennicutt et al. (2009), and although highly successful, does require some caution when low levels of star formation are measured (e.g. Boselli et al. 2015). The equivalent FUV +  $24\mu\text{m}$  SFR relation (e.g. Bigiel et al. 2008; Leroy et al. 2008; Boquien et al. 2016) was made possible by the NUV and FUV bands of the *GALEX* satellite (Martin et al. 2005). Both these relations have been used extensively to study star formation in nearby galaxies (e.g. Rahman et al. 2011; Ford et al. 2013; Momose et al. 2013; Heesen et al. 2014) and variations include: FUV +  $25\mu\text{m}$  (e.g. Hao et al. 2011), UV +  $22\mu\text{m}$  (e.g. Cortese 2012; Huang & Kauffmann 2015; Casasola et al. 2017), and  $H\alpha$  +  $22\mu\text{m}$  (e.g. Lee et al. 2013).

The *Infrared Astronomical Satellite*, *IRAS* (Neugebauer et al. 1984), *Infrared Space Observatory*, *ISO* (Kessler et al. 2003), *Spitzer Space Telescope* (Werner et al. 2004), and *Herschel Space Observatory* (Pilbratt et al. 2010) pioneered the use of monochromatic infrared SFR calibrators. In particular, the  $24\mu\text{m}$  band has been characterised by several studies for the determination of global SFRs (Wu et al. 2005; Zhu et al. 2008; Rieke et al. 2009; Calzetti et al. 2010). Tracing the warm dust continuum arising from small grains, as well as non-thermal emission from stochastically heated grains, the MIPS  $24\mu\text{m}$  band is relatively free of contamination from the stellar continuum, polycyclic aromatic hydrocarbons (PAHs), and nebular line emission, while also providing adequate spatial resolution for optically-derived surveys. In addition, warm dust emission is more closely associated with recent star formation than emission at longer wavelengths, where heating from old stellar populations become an important consideration (e.g. Popescu et al. 2000).

Indeed, with the launch of the *Wide-Field Infrared Explorer*, *WISE* (Wright et al. 2010), and its all-sky survey, the W4 band (nominally centered on  $22\mu\text{m}$ , but more recent work by Brown et al. 2014b, places the center of the band closer to  $23\mu\text{m}$ ) was expected to be the primary SFR indicator. As with the *Spitzer*  $24\mu\text{m}$  band, the *WISE* W4 band is not contaminated by emission

lines (at  $z = 0$ ), measuring the warm dust continuum which, in the absence of active galactic nucleus (AGN) activity, provides a reliable measure of star formation, comparable to that of Balmer-corrected  $H\alpha$  measures (Brown et al. 2017). However, the widespread use of this band is severely hampered due to a lack of sensitivity (Jarrett et al. 2013).

In contrast to the *WISE* 23 $\mu\text{m}$  band, which benefits from numerous *Spitzer* MIPS-24 studies, the 12 $\mu\text{m}$  window was last used extensively as part of the *IRAS* (*Infrared Astronomical Satellite*) mission, but was limited by its 4' resolution. Nevertheless, Takeuchi et al. (2005) showed that the 12 $\mu\text{m}$  luminosity could be used as a reliable measure of  $L_{\text{TIR}}$ .

Compared to the *Spitzer* mid-infrared bands, the *WISE* W3 band is somewhat unusually broad, covering 7.5 – 16.5 $\mu\text{m}$  at half-power (Jarrett et al. 2011), which at  $z = 0$  samples part of the broad 7.7 $\mu\text{m}$  PAH feature, the 8.5 $\mu\text{m}$  PAH, the 10 $\mu\text{m}$  silicate absorption feature, the 11.3 $\mu\text{m}$  PAH feature, the S(2) line of pure rotational  $\text{H}_2$  at 12.3 $\mu\text{m}$ , and the 12.81 $\mu\text{m}$  [Ne II] and 13.7 $\mu\text{m}$  [Ne III] nebular emission lines. It is sometimes characterized as the ‘‘PAH’’ band of *WISE*, because the center of the band (11.6 $\mu\text{m}$ ) is close to the 11.3 $\mu\text{m}$  emission feature, but it is clearly far more complex. PAH fractions are high in regions of active star formation and their abundance suggests that they are produced in molecular clouds (Sandstrom et al. 2010), likely growing on dust grains, but are destroyed by the relatively hard interstellar radiation field of the diffuse interstellar medium (ISM) and that produced by AGN (Smith et al. 2007).

In this paper we build on the work of Cluver et al. (2014) exploring the use of the *WISE* 12 $\mu\text{m}$  and 23 $\mu\text{m}$  bands as SFR indicators. In order to be independent of uncertainties associated with dust extinction corrections for calibrators in the UV and optical (for example, see comparison of 12 SFR metrics in Davies et al. 2016), we exploit the *Spitzer* and *Herschel* photometry of the combined SINGS (*Spitzer* Infrared Nearby Galaxy Survey; Kennicutt et al. 2003) and KINGFISH (Key Insights on Nearby Galaxies: a Far-Infrared Survey with *Herschel*; Kennicutt et al. 2011) samples to calibrate star formation determined from  $L_{\text{TIR}}$ . In addition to this sample of ‘‘typical’’ galaxies from which we derive new SFR relations, we also compare with *WISE* measurements of the most luminous infrared galaxies.

In this work, all monochromatic luminosities are defined as  $\nu L_\nu$ , for example,  $L_{12\mu\text{m}} \equiv \nu L_\nu(12\mu\text{m})$ . We adopt a Kroupa (2002) initial mass function (IMF) throughout this work, where the IMF has the slope  $\alpha = 2.3$  for stellar masses 0.5–100  $M_\odot$  and a shallower slope  $\alpha = 1.3$  for the mass range 0.1–0.5  $M_\odot$ . The cos-

mology adopted throughout this paper is  $H_0 = 70 \text{ km s}^{-1} \text{ Mpc}^{-1}$ ,  $h = H_0/100$ ,  $\Omega_M = 0.3$  and  $\Omega_\Lambda = 0.7$ . All magnitudes are in the Vega system accordant to the calibration adopted by the *WISE* survey (as described in Jarrett et al. 2011). All linear fits are performed using the Hyper-Fit package (Robotham & Obreschkow 2015) which incorporates heteroscedastic errors and outputs a measure of intrinsic scatter, as well as a parameter covariance matrix.

## 2. DATA

### 2.1. Sample

The SINGS survey (Kennicutt et al. 2003) was carried out as a Legacy Project on the *Spitzer Space Telescope* in order to study the physics of the star-forming ISM. A sample of 75 galaxies was drawn from the nearby universe ( $d < 30 \text{ Mpc}$ ) to provide spatially-resolved *Spitzer* images and spectra of a diverse set of typical local galaxies. Combined with comprehensive ancillary multi-wavelength data, a key science goal of the project was to develop improved diagnostics of SFRs in galaxies.

Building on the successes of the SINGS study, the KINGFISH project on the *Herschel Space Observatory* (Kennicutt et al. 2011) obtained far-infrared imaging and spectral line maps to enable the detailed characterisation of the ISM, as well as the heating and cooling of gaseous and dust components. The KINGFISH sample consists of a subset (57 galaxies) of the SINGS sample, with the addition of 4 galaxies: IC 0342, NGC 2146, NGC 3077 and M101 (NGC 5457). The combined SINGS/KINGFISH sample therefore consists of 79 galaxies.

### 2.2. *WISE* Photometry

The *WISE* telescope was launched in December 2009 and completed its nominal mission of an all-sky survey at 3.4, 4.6, 12 and 23 $\mu\text{m}^1$  before depleting its cryogen in October 2010. *WISE* was placed in hibernation in February 2011, but was successfully reactivated in September 2013 and continues to observe at wavelengths of 3.4 and 4.6 $\mu\text{m}$  as part of the NEOWISE program (Mainzer et al. 2014).

With a 40cm diameter primary mirror, the native image resolution of single exposure *WISE* frames is  $\approx 6''$  in W1 (3.4 $\mu\text{m}$ ) and W2 (4.6 $\mu\text{m}$ ). To preserve the native resolution and improve sensitivity by adding the latest NEOWISE imaging, we have constructed new mosaics employing the ICORE software package (Masci

<sup>1</sup> We adopt the W4 calibration from Brown et al. (2014b), in which the W4 response is redder, with a central wavelength is 22.8 $\mu\text{m}$  and the magnitude-to-flux conversion factor is 7.871 Jy.





**Figure 1.** *WISE* three-color (combined 3.4, 4.6, and 12  $\mu\text{m}$ ) images of three galaxies in the SINGS/KINGFISH sample showing the galaxies before (left) and after (right) star and background source removal. The cyan ellipses in the right panels indicate the  $1\text{-}\sigma$  isophotal apertures. In this representation, light from evolved stars is blue, while active star formation has a red color. A scale of  $2''$  is indicated with the green horizontal line, bottom left, while North is upwards and East is to the left.



2013); resulting mosaics achieve a spatial resolution of 5.9''(W1), 6.5''(W2), 7.0''(W3), and 12.4''(W4) (Jarrett et al. 2012). Consideration of the mosaic size was also of primary importance because of the angular extent of the SINGS galaxies, capturing both the galaxy, as well as the local environment to properly assess the background levels.

Target galaxies are measured using custom software optimised for performing aperture photometry on resolved galaxies (Jarrett et al. 2013; Cluver et al. 2014; Jarrett et al. 2017). Standard *WISE* photometry consists of integrated fluxes down to a  $1\sigma$  of the sky surface brightness (typically  $\sim 23$  mag arcsec $^{-2}$ ) for all four bands, which is referred to as the isophotal photometry (see Figure 1). Colors are determined using matched apertures – where apertures are all matched to the W1 isophote, except in cases where the emission is considerably less in the other bands; e.g., stellar-dominated cases, such as elliptical galaxies, with the Rayleigh-Jeans emission in W1, W2 and very little emission in W3 and W4. In those cases, we match to the smaller aperture (usually W2), and similarly for the W2–W3 color. However, for the majority of the cases, because the SINGS sample is so bright in the mid-infrared, all four bands have matched apertures. For a few rare cases (notably the dwarf galaxies), the source is not resolved in the W3 or W4 apertures, in which case we use the standard point source photometry from the ALLWISE catalogue<sup>2</sup> (Cutri et al. 2013).

The photometry pipeline also attempts to measure the total flux per band. This is carried out by modeling the axi-symmetric radial surface brightness using a Sérsic Function that fits the inner bulge light and the outer disk light. In this way, the model is integrated beyond the  $1\sigma$  isophote, extending to three disk scale lengths. The resulting total flux is typically within 5% of the isophotal flux for the W1 and W2 bands, but may be 10 to 25% larger for the W3 and W4 bands because of their relative insensitivity (Jarrett et al. 2017). Hence, when the galaxy surface brightness is well modeled, we use the total fluxes to represent the W3 and W4 integrated fluxes used for the star formation relations.

Both the W3 and W4 bands are excellent tracers of ISM emission, but they also have contributions from the evolved stellar populations. To estimate and remove this contribution, we use the method of Helou et al. (2004) in which the near-infrared band is used as a proxy for the stellar emission. Based on the SED template for a 13 Gyr galaxy (Silva et al. 1998) and the *WISE* fil-

ter transmission (Jarrett et al. 2011), we determine that 15.8% of the W1 light is contained in the W3 band, and 5.9% of the W1 light is in the W4 band. So, after scaling the W1 integrated flux densities by these factors and subtracting from the W3 and W4 total fluxes, respectively, we arrive at the ISM emission, accordingly:  $W3_{\text{PAH}}$  and  $W4_{\text{dust}}$ . Converting from flux density to luminosity then follows from  $4\pi d^2$  and scaling by the band center frequency, the so-called spectral luminosity,  $L_{12\mu\text{m}}$  and  $L_{23\mu\text{m}}$ , normalized by the solar luminosity ( $L_{\odot}$ ).

For the aggregate stellar mass, we use the GAMA-derived  $\log_{10} M_{\star}/L_{\text{W1}}$  relations from (Cluver et al. 2014), which include a W1–W2 color dependence. Here  $L_{\text{W1Sun}}$  represents the luminosity relative to the Sun, in W1, also referred to as the “in-band” luminosity (Jarrett et al. 2013). It is important not to confuse the spectral luminosity,  $\nu L_{\nu}$ , used in the SFR relations, with the in-band luminosity which is the convention for stellar mass relations.

In Table 1, we present the *WISE* measurements of 76 galaxies in the combined SINGS/KINGFISH sample, i.e. all except HoI, HoII and HoIX. These dwarf, irregular galaxies are too faint and diffuse to measure reliably with *WISE*. The table features the W1 and W2  $1\sigma$  isophotal mags (indicated by a flag value = 0) for most galaxies indicating that they are resolved, or in some isolated cases, the point-source mags (flag value = 1); and for the W3 and W4 fluxes, the “total” mags (flag value = 10) are shown when radial surface brightness solutions were possible. The brightest galaxy in the mid-infrared bands is the starburst galaxy, M82 (NGC3034), and the faintest detected is the dwarf, M81DwB.

Table 2 contains the rest-frame derived properties of the SINGS/KINGFISH sample and includes  $L_{\text{TIR}}$  determined using Equation 5 of Dale et al. (2014) i.e. combining  $8\mu\text{m}$ ,  $24\mu\text{m}$ ,  $70\mu\text{m}$ , and  $160\mu\text{m}$ , and the most recent SINGS/KINGFISH photometry (Dale et al. 2017). Here the rest frame fluxes are computed using a set of galaxy templates (Brown et al. 2014a) and SED fitting; see Jarrett et al. (2017) for more details.  $W3_{\text{PAH}}$  and  $W4_{\text{dust}}$  represent the ISM emission in the W3 and W4 bands (with the stellar emission subtracted). Spectral luminosities, used for SFRs, are indicated by  $\nu L_{\text{band}}$ ; and the W1 in-band luminosity,  $L_{\text{W1Sun}}$ , is used for the stellar mass estimation. The most luminous galaxy in our SINGS/KINGFISH sample is the peculiar NGC 2146, which is indeed classified as a luminous infrared galaxy (LIRG).

<sup>2</sup> <http://irsa.ipac.caltech.edu/cgi-bin/Gator/nph-dd>

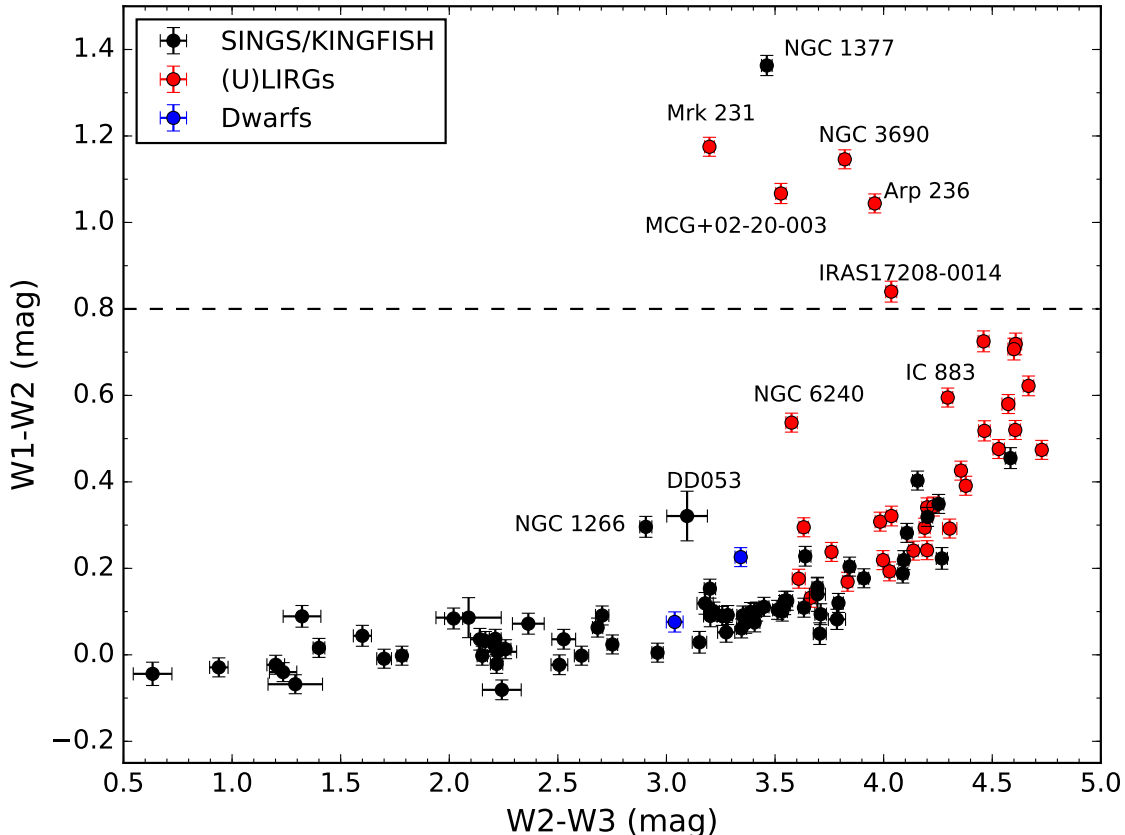


**Figure 2.** *WISE* color-color diagram of the SINGS/KINGFISH sample, as well as additional dwarfs and (U)LIRGs from the literature. Early-type galaxies with little star formation are expected to lie in the bottom left of this diagram ( $W2-W3 < 2$ ), while star-forming disk galaxies occupy the right-hand side of the diagram ( $W2-W3 > 3.5$ ). The dashed line indicates the threshold of the [Stern et al. \(2012\)](#) AGN color space; above this line, the mid-infrared emission is dominated by the heating from dusty AGN. Star-forming galaxies with little hot dust (as traced by  $W1-W2$ ) form a tight sequence in *WISE* color-color space. Galaxies lying above this trend, as well as those within the AGN color space, are labeled.

We supplement our sample with several dwarf galaxies and (Ultra) Luminous Infrared Galaxies, (U)LIRGs, drawn from *IRAS* studies (see Table 4 references), to better explore the behavior at the extremes of star-forming systems. Table 3 lists thirty-two (U)LIRGS and their *WISE* measurements. The  $L_{\text{TIR}}$  values from the literature, restframe and derived properties are given in Table 4. A mix of star-forming, AGN, and hybrids thereof comprise this sample of (U)LIRGS. The requirement of dwarf galaxies to be well-measured in *WISE*, and have reliable  $L_{\text{TIR}}$  from the literature, limits the sample to the two listed in Table 5, with their derived quantities given in Table 6.

### 3. RESULTS

#### 3.1. *WISE* colors

The *WISE* color-color diagram, shown in Figure 2, is a useful diagnostic tool for determining the underlying characteristics of a given sample ([Wright et al. 2010](#);

[Jarrett et al. 2011](#)). As in Figure 11 of [Jarrett et al. \(2017\)](#), the  $W2-W3$  color can be used as a broad proxy for morphology: galaxies with a color  $< 2$  are typically spheroids (with little star formation), while star-forming disks usually have a color  $> 3.5$ . On the other hand, the  $W1-W2$  color acts as a proxy for AGN activity; elevated  $W1-W2$  colors compared to the intrinsically tight trend typically indicate the presence of an AGN causing an excess of hot dust emission ([Stern et al. 2012](#)). In the case of our sample, the colors clearly define a star-forming sequence from dust-free (early types) to active star-formers (late-types).

Deviations arise from extreme activity, either star formation or AGN, or a combination of both (ULIRGs stand out in this way). For example, NGC 1266 is known to harbor an AGN ([Alatalo et al. 2011](#)) and this is likely why it sits slightly above the general trend in color space. Pointing to a separate issue, the elevated color of the dwarf galaxy DD053 is likely the re-



sult of contamination from a background source, located at 08h43m07.1s +66°10'57", which has the characteristic color of an AGN. The source of its W1–W2 color is therefore ambiguous.

An interesting case, the massive lenticular NGC 1377 is the only galaxy in the SINGS/KINGFISH sample with W1–W2 > 0.8 indicating a global color dominated by emission from the dusty torus of an AGN. The W1–W2 color is itself not a definitive discriminator of the presence or absence of an AGN (Gürkan et al. 2014), but elevated W1–W2 colors indicate excess hot dust emission from an AGN with W1–W2 > 0.8 implying global galaxy colors dominated by this emission. We would therefore expect the W3 and W4 luminosity, sensitive to star formation, to be contaminated by AGN emission.

NGC 1377 is an extreme far-infrared excess galaxy (Roussel et al. 2003) and has to date been considered to be a young, dusty starburst (Roussel et al. 2006) due to being an extreme (low) outlier in the radio-infrared correlation. However, recent ALMA, JVLA and *Chandra* observations suggest it is harbouring an extremely obscured AGN with a molecular jet (Aalto et al. 2016; Costagliola et al. 2016). Moreover, *Spitzer* IRS spectroscopy shows a steep, strong continuum with the largest silicate opacity of any SINGS source (Smith et al. 2007). In this instance, the *WISE* colors of the integrated emission supports the scenario of an obscured AGN.

The underlying heating source in cases such as these, where mid-infrared diagnostic emission lines are swamped by the continuum, will be ambiguous in the absence of other diagnostics – in this case *WISE* colors. For this reason, NGC 1377 is excluded from the star formation calibration determination in the next Section.

Unsurprisingly, several local (U)LIRGs show evidence of AGN-dominated (e.g. Mrk 231) or AGN-contaminated (e.g. NGC 6240) colors. For the remainder of this study we refer to the AGN-dominated *WISE* color (U)LIRG systems, i.e. with W1–W2 colors above the Stern et al. (2012) line, as “AGN (U)LIRGs”, with the caveat that we cannot determine if extreme star-formation or AGN-heating is the dominant emission mechanism for these sources.

### 3.2. *WISE* Star Formation Rates: Relations and Performance

In this Section we explore the behavior of the *WISE* W3 (12 $\mu$ m) and W4 (23 $\mu$ m) luminosities as a measure of star formation for the SINGS/KINGFISH sample. Figure 3 shows the  $L_{\text{TIR}}$  values plotted as a function of the  $L_{12\mu\text{m}}$  and  $L_{23\mu\text{m}}$  luminosities, respectively (here and throughout,  $L_{12\mu\text{m}}$  and  $L_{23\mu\text{m}}$  refer to  $\nu L_\nu(12\mu\text{m})$  and

$\nu L_\nu(23\mu\text{m})$ , respectively). The location of the (U)LIRG sample and additionally measured dwarf galaxies is also shown. For the  $L_{\text{TIR}}$  vs  $L_{12\mu\text{m}}$  diagram, a tight linear trend is observed, even down to low luminosities ( $\sim 10^6 L_\odot$ ). A best fit is given by:

$$\begin{aligned} \log L_{\text{TIR}}(L_\odot)(M_\odot \text{ yr}^{-1}) = \\ (0.889 \pm 0.018) \log L_{12\mu\text{m}}(L_\odot) + (2.21 \pm 0.15), \end{aligned} \quad (1)$$

with a 1- $\sigma$  scatter of 0.15 dex.

At the high luminosity ( $> 10^{10.5} L_\odot$ ) end, however, the (U)LIRG sample tends towards higher values of  $L_{\text{TIR}}$ , i.e. the W3 band is under-luminous. This suggests additional heating not being traced by the W3 band, or alternatively, the effect of strong silicate absorption in the W3 band. Curiously, the most luminous source in the entire ensemble, Mrk 231, a dusty and gas-rich broad-line QSO, falls exactly on the relation derived from star-forming galaxies several orders of magnitude less luminous.

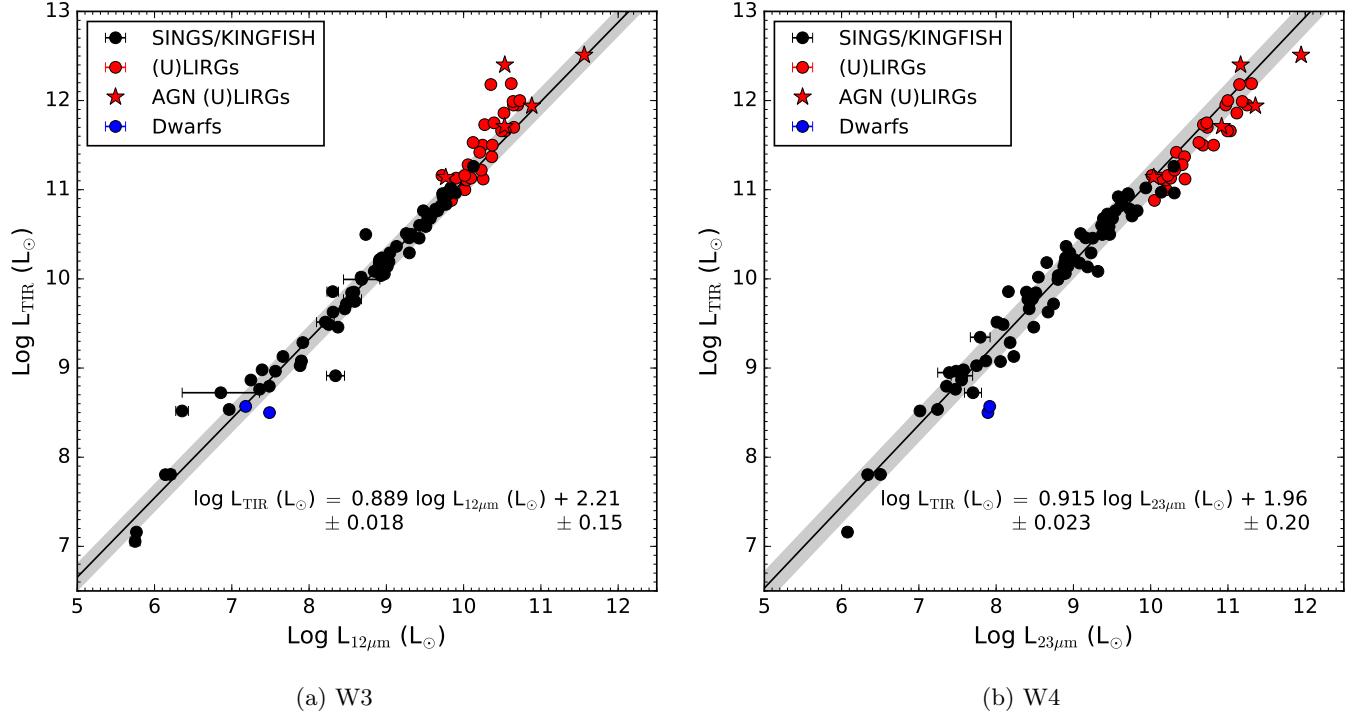
In contrast to the W3 band, comparison of the  $L_{23\mu\text{m}}$  luminosities to  $L_{\text{TIR}}$  shows increased scatter, and the opposite behavior with extreme galaxies, i.e. the  $L_{23\mu\text{m}}$  luminosity is over-luminous compared to the  $L_{\text{TIR}}$  values for (U)LIRGs. This suggests that the W4 band has enhanced continuum emission relative to the far-infrared, likely boosted by dust-obscured AGN. The best fit relation for the SINGS/KINGFISH sample is:

$$\begin{aligned} \log L_{\text{TIR}}(L_\odot)(M_\odot \text{ yr}^{-1}) = \\ (0.915 \pm 0.023) \log L_{23\mu\text{m}}(L_\odot) + (1.96 \pm 0.20), \end{aligned} \quad (2)$$

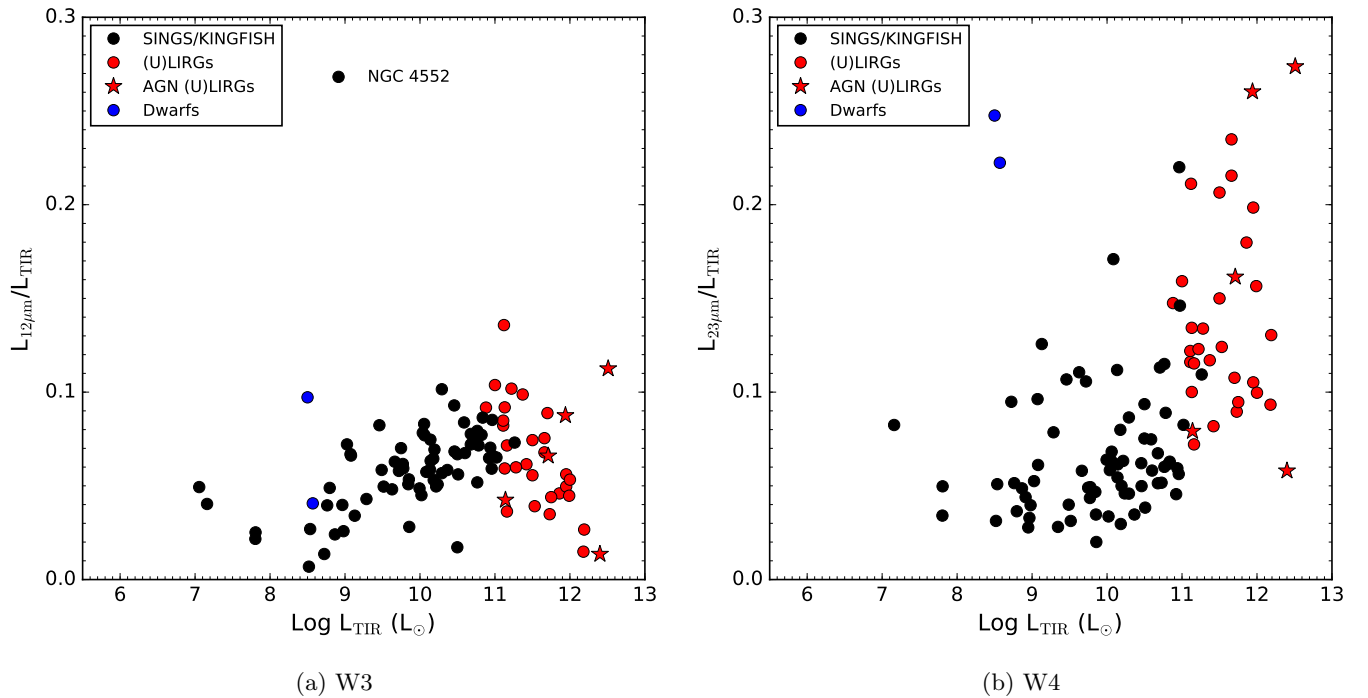
with a 1- $\sigma$  scatter of 0.18 dex.

Figure 4 examines the ratio of the *WISE* bands to  $L_{\text{TIR}}$  as a function of increasing  $L_{\text{TIR}}$ . In Figure 4a, NGC 4552 (Messier 89) is a clear outlier; it is an elliptical galaxy in the Virgo Cluster with little or no star formation (e.g. Shapiro et al. 2010), but with an infrared excess at 12 $\mu$ m relative to a dust-free elliptical (Brown et al. 2014a), detected by *Herschel* (di Serego Alighieri et al. 2013), and containing a “mini-AGN” (Cappellari et al. 1999). More distant galaxies of this type would not have a W3 detection.

Comparing Figure 4a and b, the W3 band shows a more constant response compared to W4, where higher  $L_{\text{TIR}}$  produces correspondingly more 23 $\mu$ m emission. For W3, we see the (U)LIRG population turning over, unlike what is observed for W4 where the  $L_{23\mu\text{m}}/L_{\text{TIR}}$



**Figure 3.**  $L_{\text{TIR}}$  as a function of a)  $L_{12\mu\text{m}}$  and b)  $L_{23\mu\text{m}}$  for the SINGS/KINGFISH sample, as well as the added (U)LIRG and dwarf sample (see text). For most points, the error on  $L_{12\mu\text{m}}$  is smaller than the data point. The fit to the SINGS/KINGFISH sample is shown as the solid black line with the 1- $\sigma$  scatter indicated by the shaded region (0.15 for  $L_{12\mu\text{m}}$  and 0.18 for  $L_{23\mu\text{m}}$ ).



**Figure 4.** The ratio of a)  $L_{12\mu\text{m}}/L_{\text{TIR}}$  and b)  $L_{23\mu\text{m}}/L_{\text{TIR}}$  as a function of  $L_{\text{TIR}}$  shows the variation of the contribution from a) W3, and b) W4 as the total infrared luminosity increases. The W3 luminosity shows a more constant response compared to the W4 luminosity

ratio appears to *increase*. This could be the result of

silicate absorption in W3 preventing the continuum at  $12\mu\text{m}$  from gaining power relative to  $L_{\text{TIR}}$ .



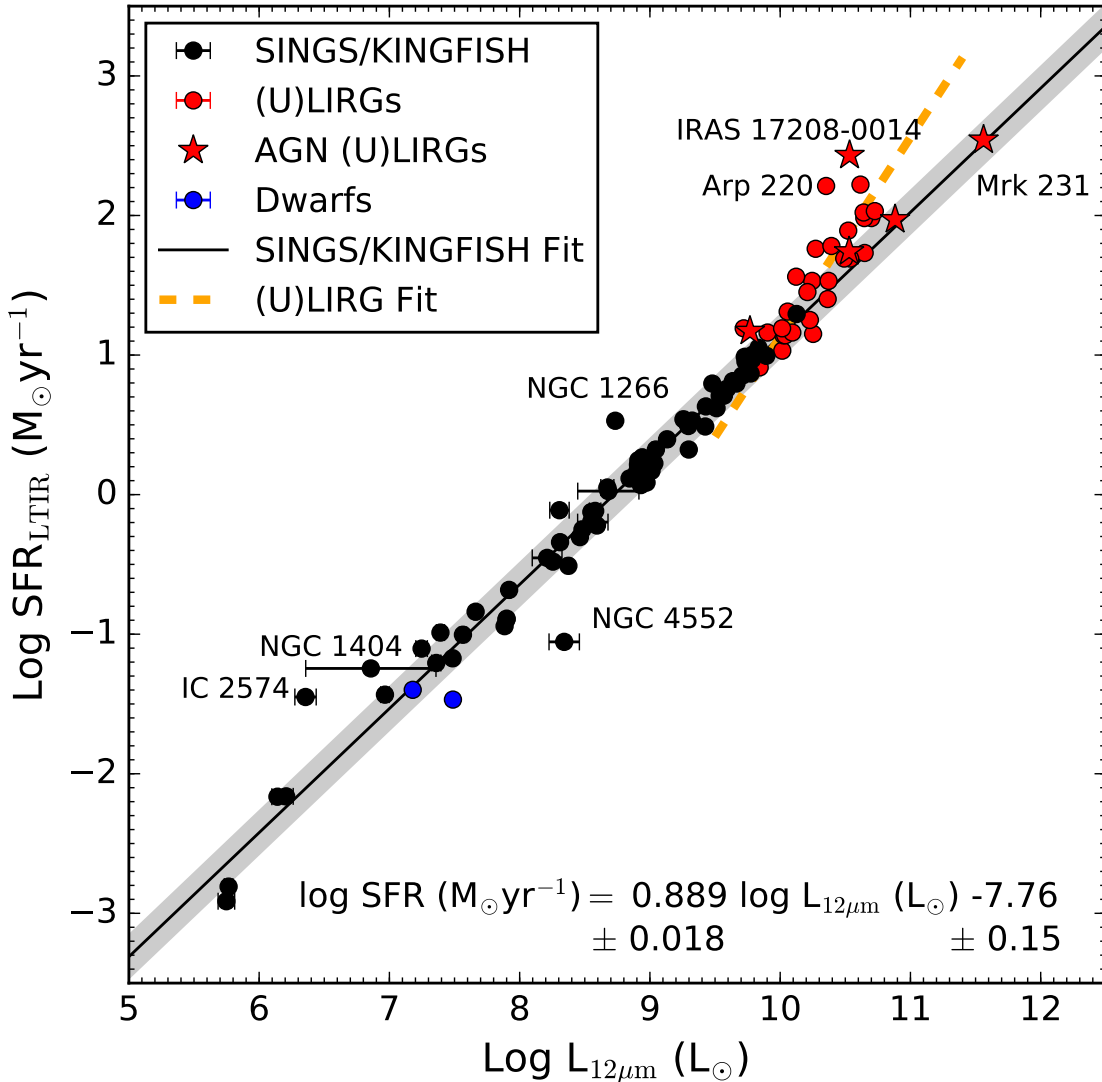


**Figure 5.**  $L_{\text{TIR}}$ -derived star formation rates are plotted against the *WISE* W3  $12\mu\text{m}$  luminosity and the best fit line to the SINGS/KINGFISH sample is shown (solid line); the  $1\text{-}\sigma$  scatter is indicated by the shaded region (0.15 dex). For comparison, a sample of (U)LIRGs and dwarf galaxies are also shown. A fit to the (U)LIRG sample is shown by the dashed line and is given by:  $\log \text{SFR} (M_{\odot} \text{yr}^{-1}) = (1.430 \pm 0.161) \log L_{12\mu\text{m}} (L_{\odot}) - (13.17 \pm 1.66)$  with a  $1\text{-}\sigma$  scatter of 0.22 dex. The trend suggests that  $L_{\text{TIR}}$  gives a higher SFR compared to the W3-derived value for high luminosity sources.

Figure 4b suggests that for  $L_{\text{TIR}} > 10^{11} L_{\odot}$ , the fractional power traced by W4 (the heating of small dust grains) compared to  $L_{\text{TIR}}$  increases rapidly.

In the next step, we calibrate the W3 and W4 spectral luminosities of the SINGS/KINGFISH sample to star formation rates (SFRs) determined from the total infrared luminosity,  $L_{\text{TIR}}$ . The SFR is determined using Equation 1.3 in Calzetti (2013), which uses the Starburst99 (Leitherer et al. 1999) models assuming solar

metallicity, constant star formation over  $\tau = 100\text{Myr}$ , and a Kroupa IMF, as follows:

$$\text{SFR}(M_{\odot} \text{yr}^{-1}) = 2.8 \times 10^{-44} L_{\text{TIR}}(\text{erg.s}^{-1}) \quad (3)$$

We note that this calibration assumes that the stellar emission, most notably the UV component, is entirely absorbed and re-radiated at infrared wavelengths, which constitutes an upper limit to what would occur in a real galaxy. Comparison of this relation to that of Murphy et al. (2011), who also use the Starburst99 models, yields a negligible difference.

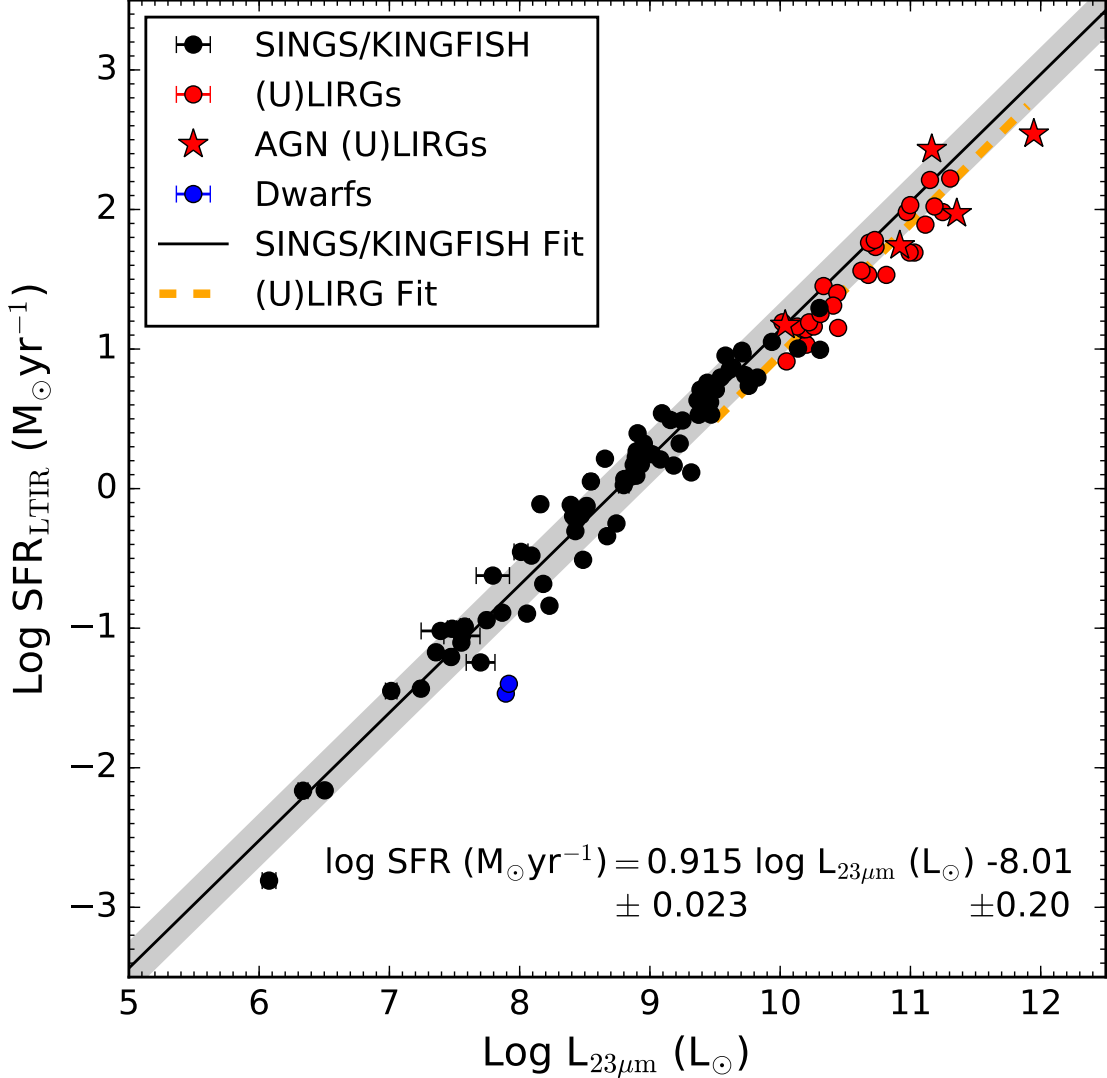


**Figure 6.**  $L_{\text{TIR}}$ -derived star formation rates are plotted as a function of *WISE* W4  $23\mu\text{m}$  luminosity. The best fit line to the SINGS/KINGFISH sample is shown as a solid line and has a  $1\text{-}\sigma$  scatter of 0.18 dex (indicated by the shaded region). A fit to the (U)LIRG sample (dashed line) is given by:  $\log \text{SFR} (M_{\odot} \text{yr}^{-1}) = (0.938 \pm 0.062) \log L_{23\mu\text{m}}(L_{\odot}) - (8.42 \pm 0.66)$  with a  $1\sigma$  scatter of 0.13 dex. This suggests that W4 is marginally overestimating the SFR compared to  $L_{\text{TIR}}$  at high luminosity.

In Figure 5 we relate the SFR derived from  $L_{\text{TIR}}$  (using Equation 1) to the  $L_{12\mu\text{m}}$  luminosity and show the best fit to the SINGS/KINGFISH sample. The resulting fit is given by:

$$\log \text{SFR} (M_{\odot} \text{yr}^{-1}) = (0.889 \pm 0.018) \log L_{12\mu\text{m}}(L_{\odot}) - (7.76 \pm 0.15), \quad (4)$$

with a  $1\text{-}\sigma$  scatter of 0.15 dex.

The overall trend is tight, with the exception of the outliers: NGC 1266, NGC 4552, and IC 2574. In the case of NGC 1266, the AGN activity is likely producing

excess dust heating compared to what is traced in W3. The offset location of the dwarf irregular, IC 2574, could be due to the strong variations in dust temperature and characteristics found across the galaxy due to triggered star formation (Cannon et al. 2005).

The (U)LIRGs overplotted on Figure 5 show a trend to higher SFRs than what is seen for the fit to the SINGS/KINGFISH sample. A best fit to only the (U)LIRG sample is given by:



$$\begin{aligned} \log \text{SFR} (M_{\odot} \text{ yr}^{-1}) = \\ (1.430 \pm 0.161) \log L_{12\mu\text{m}}(L_{\odot}) - (13.17 \pm 1.66), \end{aligned} \quad (5)$$

with a  $1\text{-}\sigma$  scatter of 0.22 dex.

This suggests that the  $12\mu\text{m}$  luminosity is underestimated compared to  $L_{\text{TIR}}$  (see also Figure 3a) for the (U)LIRGs. The W3 band is sensitive to the silicate absorption feature expected to be common in the dusty, embedded starbursts powering the infrared emission of the (U)LIRGs and this likely diminishes the  $L_{12\mu\text{m}}$  compared to  $L_{\text{TIR}}$ .

Although the center of the W3 band is close to the  $11.3\mu\text{m}$  PAH feature, the breadth of the band samples several features, as well as the continuum from warm, large grains and stochastically heated grains. On average, the total PAH emission in the band only accounts for  $\sim 34\%$  of the  $12\mu\text{m}$  flux (see Appendix A). Although associated with star formation, the strong radiation fields associated with nuclear starbursts and/or AGN would likely suppress PAH emission close in, where molecules are less shielded than they would be in a star-forming disk, however the hot dust would boost the continuum being traced by W3. Therefore the advantage of the  $12\mu\text{m}$  *WISE* band as a SFR indicator appears to be its breadth thus sampling a mix of PAHs, nebular lines and continuum.

In Figure 6, a fit is derived between the  $L_{\text{TIR}}$ -derived SFR and the  $L_{23\mu\text{m}}$  luminosities of the SINGS/KINGFISH sample. The resulting fit is given by:

$$\begin{aligned} \log \text{SFR} (M_{\odot} \text{ yr}^{-1}) = \\ (0.915 \pm 0.023) \log L_{23\mu\text{m}}(L_{\odot}) - (8.01 \pm 0.20), \end{aligned} \quad (6)$$

with a  $1\text{-}\sigma$  scatter of 0.18 dex.

In the case of  $23\mu\text{m}$  luminosity, a fit to the (U)LIRGs is given by:

$$\begin{aligned} \log \text{SFR} (M_{\odot} \text{ yr}^{-1}) = \\ (0.938 \pm 0.062) \log L_{23\mu\text{m}}(L_{\odot}) - (8.42 \pm 0.66), \end{aligned} \quad (7)$$

with a  $1\text{-}\sigma$  scatter of 0.13 dex. This indicates a marginal trend to lower SFRs than what is seen for the fit to the SINGS/KINGFISH sample, possibly due to increased  $23\mu\text{m}$  emission due to obscured AGN activity or embedded star formation.

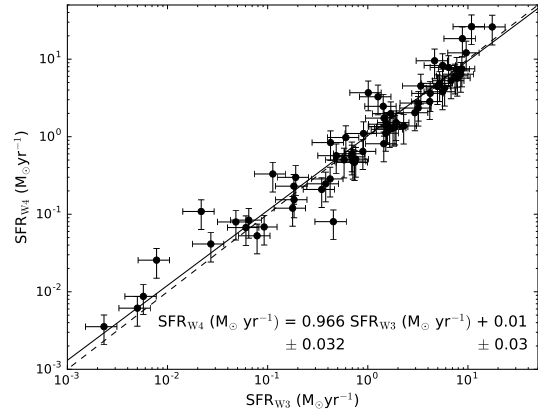


**Figure 7.** W3-derived SFR compared to the W4-derived SFR for the SINGS/KINGFISH sample indicates that overall the mid-infrared SFRs are consistent. A fit to the points is given by the solid line (with  $1\text{-}\sigma$  scatter of 0.0001 dex) and a one-to-one (dashed) shown for comparison.

Comparing the fits of Figure 5 and 6, the  $12\mu\text{m}$  relation appears to have less scatter and hold over 5 orders of magnitude of  $12\mu\text{m}$  luminosity. The W4 band, which is dominated by the warm dust continuum, shows increased scatter and appears more curved (or at least, a strong break) at the extreme (LIRG) end, which agrees with Figure 4b.

In Figure 7 we compare the SFRs for the SINGS/KINGFISH sample determined using Equations 2 and 3, respectively. Although the points show some scatter, overall they are consistent with respect to the one-to-one relation over several orders of magnitude of SFR. A fit to the points is given by:

$$\begin{aligned} \text{SFR}_{\text{W4}} (M_{\odot} \text{ yr}^{-1}) = \\ (0.966 \pm 0.032) \text{SFR}_{\text{W3}} (M_{\odot} \text{ yr}^{-1}) + (0.01 \pm 0.03), \end{aligned} \quad (8)$$

with a  $1\text{-}\sigma$  scatter of 0.0001 dex.

Finally, we explore the effect of metallicity on, in particular, the  $L_{12\mu\text{m}}$  luminosity relation. Since PAH features can be affected by the strong radiation fields associated with low metallicity systems (Smith et al. 2007) and given the contribution of PAHs to the W3 band, we color code the galaxies in the SINGS/KINGFISH sample according to their oxygen [O/H] metallicities, as given by Moustakas et al. (2010). In Figure 8a the abundances are calculated (where possible) using the Kobulnicky & Kewley (2004) calibration, whereas in 12b, the metallicity is estimated from the B-band luminosity (and is therefore available for all galaxies in the SINGS/KINGFISH sample). From Figure 8 it is evident that for the metallicities probed in this sample,

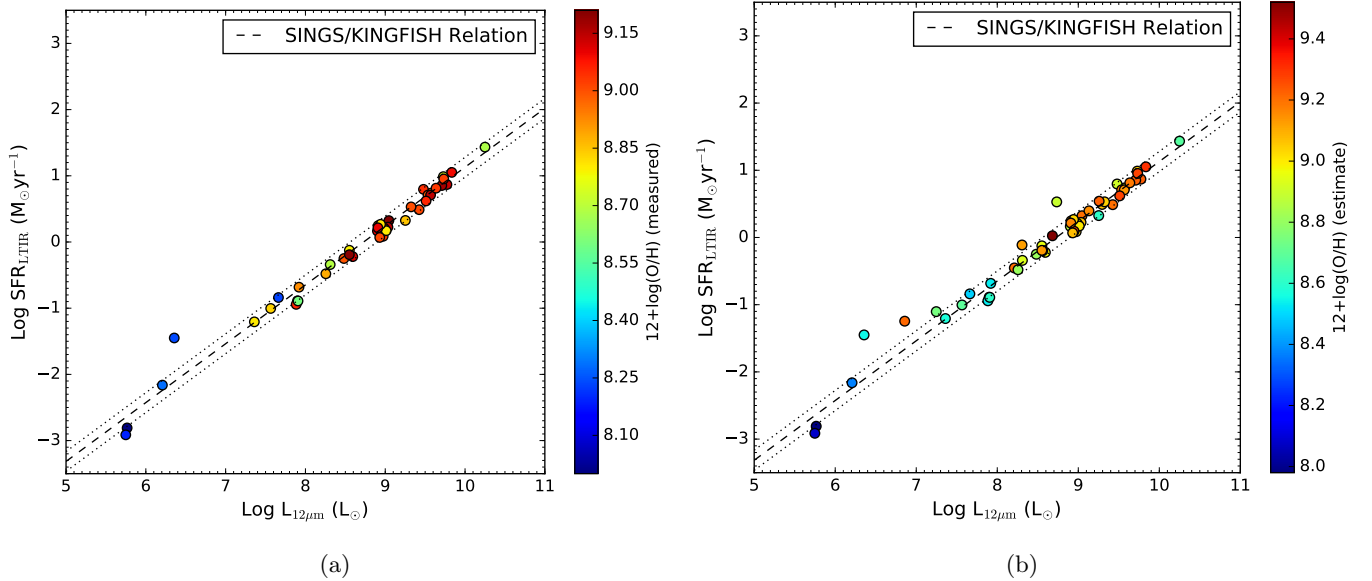


**Figure 8.** SINGS/KINGFISH galaxies color-coded by metallicity: in a) showing abundances determined using characteristic (global) abundances from Moustakas et al. (2010) using the Kobulnicky & Kewley (2004) calibration, and b) metallicity estimate from Moustakas et al. (2010) derived from the B-band luminosity-metallicity relation, using the Kobulnicky & Kewley (2004) calibration. The dotted lines show the  $1\text{-}\sigma$  scatter around the SFR relation (dashed line); the W3 band ( $L_{12\mu\text{m}}$ ) does not appear sensitive to the metallicity of the galaxy.

there does not appear to be a systematic effect on the SINGS/KINGFISH  $L_{12\mu\text{m}}$  SFR relation. However, we do not expect this SFR calibration to hold for lower metallicity environments.

### 3.3. Comparison to other WISE SFR relations

In Figure 9 we compare the SFR relations derived in Section 3.2 to those in the literature that similarly make use of WISE resolved source photometry. We list in Table 7 and Table 8, the source of these relations for W3 and W4, respectively, the calibrators used and the adopted IMF. Apart from the Brown et al. (2017) relation where a conversion to a Kroupa (2002) IMF has been applied, we have made no attempt to take into account differences in IMF and calibrator in order to illustrate the breadth of uncertainty in any given SFR, depending on the chosen relation. See Brown et al. (2017) for a broader listing of SFR relations from the literature.

The differences due to using either the W3 or W4 band are also apparent. For W4, relations calibrated against  $H\alpha$ -derived SFRs (Cluver et al. 2014; Catalán-Torrecilla et al. 2015; Brown et al. 2017) appear to agree within the expected scatter. However, the W3 relations show little consistency, suggesting that the choice of sample and calibrator may cause significant variation.

### 3.4. Comparison to other wavelengths

In this Section we compare the  $12\mu\text{m}$ - and  $23\mu\text{m}$ -derived SFRs, using Equations 2 and 3, respectively,

to SFRs derived using  $H\alpha+24\mu\text{m}$ , radio continuum and UV+IR measurements.

In Kennicutt et al. (2009) the authors provide a hybrid calibration that combines observed  $H\alpha$  and  $24\mu\text{m}$  luminosities as a proxy for dust attenuation-corrected  $H\alpha$ . We use the  $H\alpha$  fluxes given in Kennicutt et al. (2009) for the SINGS galaxies and combine them with the *Spitzer* MIPS  $24\mu\text{m}$  fluxes given by Dale et al. (2017). In addition, we use the  $H\alpha$  spectro-photometric fluxes for 15 SINGS galaxies included in Moustakas & Kennicutt (2006). Employing the mid-infrared Kennicutt et al. (2009) coefficient that corrects  $H\alpha$  for attenuation, in Figure 11a we compare the combined  $H\alpha$  and  $24\mu\text{m}$  luminosities to the  $12\mu\text{m}$  luminosities and find a linear fit for the  $H\alpha$  sample given by:

$$\begin{aligned} \log(L_{H\alpha} + 0.02 * L_{24\mu\text{m}}) \text{ erg.s}^{-1} = \\ (0.686 \pm 0.018) \log L_{12\mu\text{m}}(\text{erg.s}^{-1}) + (11.92 \pm 1.52), \end{aligned} \quad (9)$$

with a  $1\text{-}\sigma$  scatter of 0.26 dex. We note that although there is considerable scatter, the WISE W3 luminosity is proportional to the  $H\alpha$  luminosity over nearly 3 orders of magnitude. Comparison of this relation to that of Brown et al. (2017), which compares  $L_{12\mu\text{m}}$  to that of Balmer Decrement extinction-corrected  $H\alpha$ , we find that our relation is marginally flatter, but broadly consistent.

**Table 7.** Comparison of W3 SFR Relations

Reference	Calibrator	SFR Conversion	Adopted IMF
Jarrett et al. (2013)	24 $\mu$ m	Rieke et al. (2009)	Rieke et al. (1993)
Cluver et al. (2014)	H $\alpha$	Wijesinghe et al. (2011)	Baldry & Glazebrook (2003)
Davies et al. (2016)	Radiative Transfer	Grootes et al. (2017)	Chabrier (2003)
Brown et al. (2017)	H $\alpha$	Kennicutt et al. (2009)	Chabrier (2003)

**Table 8.** Comparison of W4 SFR Relations

Reference	Calibrator	SFR Conversion	Adopted IMF
Jarrett et al. (2013)	24 $\mu$ m	Rieke et al. (2009)	Rieke et al. (1993)
Cluver et al. (2014)	H $\alpha$	Wijesinghe et al. (2011)	Baldry & Glazebrook (2003)
Catalán-Torrecilla et al. (2015) <sup>a</sup>	H $\alpha$	Kennicutt et al. (2009)	Kroupa (2002)
Davies et al. (2016)	Radiative Transfer	Grootes et al. (2017)	Chabrier (2003)
Brown et al. (2017)	H $\alpha$	Kennicutt et al. (2009)	Chabrier (2003)

NOTE—<sup>a</sup> The log-scale fit is used here for comparison.

Using the conversion to SFR, assuming a Kroupa IMF, given by Kennicutt et al. (2009), i.e.

$$\text{SFR}(M_{\odot} \text{ yr}^{-1}) = 5.5 \times 10^{-42} [L(\text{H}\alpha_{\text{obs}}) + 0.02 * L_{24\mu\text{m}}] (\text{erg.s}^{-1}) \quad (10)$$

allows us to compare SFR relations (Figure 10). The linear best-fit is given by:

$$\text{SFR}(L(\text{H}\alpha_{\text{obs}}) + 0.02 * L_{24\mu\text{m}}) (M_{\odot} \text{ yr}^{-1}) = (0.776 \pm 0.041) \text{SFR}_{12\mu\text{m}} (M_{\odot} \text{ yr}^{-1}) - (0.30 \pm 0.04), \quad (11)$$

with a 1- $\sigma$  scatter of 0.23 dex.

The distribution of points and best-fit relation shows a systematic effect where the 12 $\mu$ m-derived SFRs (using Equation 2) are higher than those given by H $\alpha$  + 24 $\mu$ m for SFRs > 0.1 M $_{\odot}$ yr $^{-1}$ .

In Figure 11 we show the comparison with 23 $\mu$ m instead of 12 $\mu$ m. The H $\alpha$  + 24 $\mu$ m luminosities as a function of  $L_{23\mu\text{m}}$  (Figure 11a) show a clear linear trend given by:

$$\log(L_{\text{H}\alpha} + 0.02 * L_{24\mu\text{m}}) \text{ erg.s}^{-1} = (0.760 \pm 0.027) \log L_{12\mu\text{m}} (\text{erg.s}^{-1}) + (8.79 \pm 1.13), \quad (12)$$

with a 1- $\sigma$  scatter of 0.18 dex. Note the much tighter relation of W4 with H $\alpha$  + 24 $\mu$ m as compared to that with W3.

Using the same SFR conversion for  $L_{\text{H}\alpha} + 0.02 * L_{24\mu\text{m}}$  as above, and the *WISE* 23 $\mu$ m relation given by Equation (4), we find that the SFRs are related by the equation:

$$\text{SFR}(L(\text{H}\alpha_{\text{obs}}) + 0.02 * L_{24\mu\text{m}}) (M_{\odot} \text{ yr}^{-1}) = (0.832 \pm 0.029) \text{SFR}_{12\mu\text{m}} (M_{\odot} \text{ yr}^{-1}) - (0.30 \pm 0.03), \quad (13)$$

with a 1- $\sigma$  scatter of 0.10 dex.

The tightness in the relation is likely at least partially due to the similarities between the *WISE* 23 $\mu$ m and the

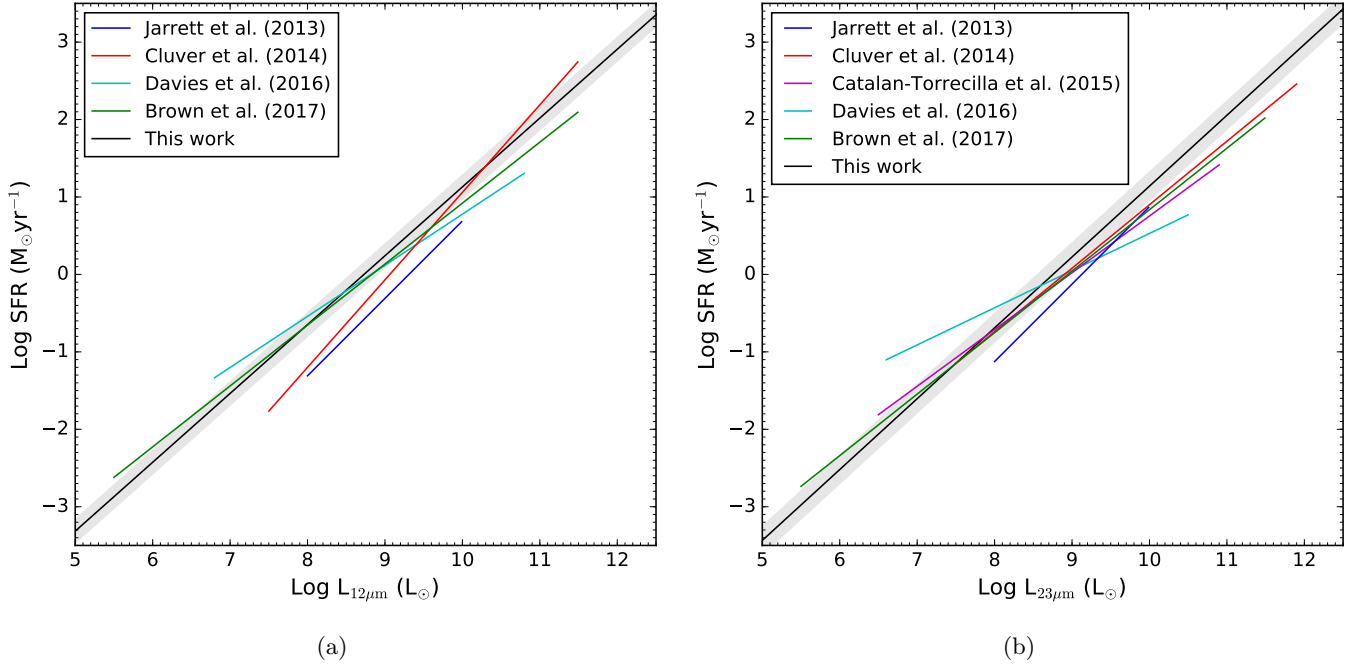


**Figure 9.** The a)  $L_{12\mu\text{m}}$  (W3) and b)  $L_{23\mu\text{m}}$  (W4) SFR relation from this work compared to existing relations from the literature using different calibrators and IMFs (see Table 7 and Table 8). This plot illustrates the (often hidden) complexities in applying SFR relations that differ in methodology and sample selection.

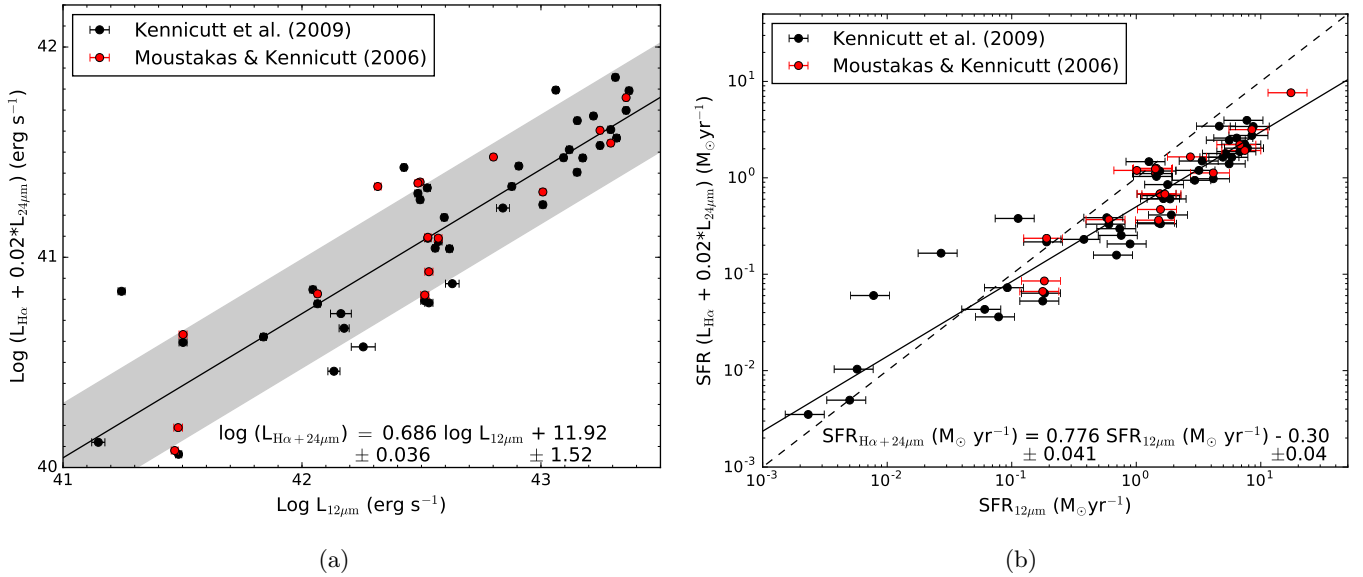


**Figure 10.** Comparing  $\text{H}\alpha + 24\mu\text{m}$  luminosities to  $L_{12\mu\text{m}}$  in (a) shows a linear trend for galaxies using  $\text{H}\alpha$  measurements from Kennicutt et al. (2009) (black points) with a  $1\text{-}\sigma$  scatter of 0.26 dex. Using galaxies where the  $\text{H}\alpha$  measurements are drawn from Moustakas & Kennicutt (2006) (red points) follows a similar distribution. In (b) we compare the SFRs derived using  $\text{H}\alpha + 24\mu\text{m}$  to those derived using the  $12\mu\text{m}$  relation given by Equation (3). A one-to-one relation (dashed line) indicates the  $12\mu\text{m}$ -derived SFRs are systematically higher than those from  $\text{H}\alpha + 24\mu\text{m}$  for  $\text{SFR} > 0.1 \text{ M}_{\odot}\text{yr}^{-1}$ . The  $1\text{-}\sigma$  scatter of the best-fit relation (solid line) is 0.23 dex.



MIPS  $24\mu\text{m}$  band such that the x and y axes are not fully independent of each other. As in Figure 10b, Figure 11b shows that the *WISE*-derived SFR is systematically higher than what the  $\text{H}\alpha+24\mu\text{m}$  predicts (for  $\text{SFR} > 0.1 M_{\odot}\text{yr}^{-1}$ ). Since the luminosities agree so well, the SFR differences are therefore due to the scaling between luminosity (e.g.,  $L_{\text{TIR}}$ ) and SFR.

Next we explore how the *WISE*-derived SFRs compare to those using 20cm radio continuum observations. For the SINGS/KINGFISH sample we use the 20cm fluxes from Dale et al. (2017), where available, except for NGC 584 whose flux is taken from Brown et al. (2011), NGC 1512 from Koribalski & López-Sánchez (2009), NGC 3077 from Condon et al. (1998), Mrk 33 from Bravo-Alfaro et al. (2004), and NGC 5195 from Condon et al. (2002). To convert to a radio continuum SFR, we employ the relation (Equation 17) of Murphy et al. (2011); this also assumes a Kroupa IMF. The comparison is shown in Figure 12, with the  $12\mu\text{m}$  SFR comparison in panel (a) and the  $23\mu\text{m}$  comparison in (b). The fit for the  $12\mu\text{m}$  comparison is given by:

$$\begin{aligned} \text{SFR}_{12\mu\text{m}} (M_{\odot}\text{yr}^{-1}) = \\ (0.871 \pm 0.046) \text{SFR}_{20\text{cm}} (M_{\odot}\text{yr}^{-1}) + (0.14 \pm 0.04), \end{aligned} \quad (14)$$

with a  $1\text{-}\sigma$  scatter of 0.26 dex.

Although the distribution of points in Figure 12a and b appear different (with a clear outlier of NGC 4552 in Figure 12b), we obtain a very similar fit for the  $23\mu\text{m}$  relation, given by:

$$\begin{aligned} \text{SFR}_{23\mu\text{m}} (M_{\odot}\text{yr}^{-1}) = \\ (0.854 \pm 0.047) \text{SFR}_{20\text{cm}} (M_{\odot}\text{yr}^{-1}) + (0.15 \pm 0.04), \end{aligned} \quad (15)$$

with a  $1\text{-}\sigma$  scatter of 0.26 dex.

In addition, both Figure 12a and b indicate a similar behavior compared to the one-to-one relation (dashed lines) where concordance appears closest for  $\text{SFRs} > 1 M_{\odot}\text{yr}^{-1}$  with increasing scatter towards lower SFR. However, with so few data points at low SFRs, comparisons in this regime are unadvisable.

Heesen et al. (2014) used 17 THINGS (The HI Nearby Galaxy Survey; Walter et al. 2008) galaxies, observed as part of the Westerbork Synthesis Radio Telescope (WRST) SINGS sample, (Braun et al. 2007) to investigate the spatially resolved radio continuum (22cm)

SFR compared to a “hybrid” combination of *GALEX* FUV and *Spitzer*  $24\mu\text{m}$  maps, tracing unobscured and obscured star formation, respectively. We use their integrated star formation rates for galaxies in common to our SINGS/KINGFISH sample (14 galaxies) for comparison and plot the *WISE*-derived SFRs versus radio continuum SFRs in Figure 13, and the comparison to the “hybrid” SFR in Figure 14.

The best fit SFR relation in Figure 13a is given by:

$$\begin{aligned} \text{SFR}_{12\mu\text{m}} (M_{\odot}\text{yr}^{-1}) = \\ (0.842 \pm 0.072) \text{SFR}_{22\text{cm}} (M_{\odot}\text{yr}^{-1}) + (0.21 \pm 0.04), \end{aligned} \quad (16)$$

with a  $1\text{-}\sigma$  scatter of  $3.9\text{e}^{-5}$  dex,  
and for Figure 13b:

$$\begin{aligned} \text{SFR}_{23\mu\text{m}} (M_{\odot}\text{yr}^{-1}) = \\ (0.845 \pm 0.087) \text{SFR}_{22\text{cm}} (M_{\odot}\text{yr}^{-1}) + (0.12 \pm 0.05), \end{aligned} \quad (17)$$

with a  $1\text{-}\sigma$  scatter of  $1.5\text{e}^{-5}$  dex.

Comparing these to Equations (14) and (15), respectively, we note the similarity of the *WISE*-radio continuum SFR relations, the only marked difference being the very small scatter reflected by Figure 13 a and b. In addition, we see a remarkably similar behavior when considering the one-to-one relation, with the  $12\mu\text{m}$ - and  $23\mu\text{m}$ -derived SFRs systematically tending towards higher values of SFR as the SFR decreases.

In Figure 14 we consider the “hybrid” SFR indicator of FUV+ $24\mu\text{m}$ , which shows remarkably close correspondence to a one-to-one relation.

The best fit SFR relation in Figure 14a is given by:

$$\begin{aligned} \text{SFR}_{12\mu\text{m}} (M_{\odot}\text{yr}^{-1}) = \\ (1.027 \pm 0.144) \text{SFR}_{\text{FUV}+24\mu\text{m}} (M_{\odot}\text{yr}^{-1}) + (0.04 \pm 0.07), \end{aligned} \quad (18)$$

with a  $1\text{-}\sigma$  scatter of 0.19 dex,  
and for Figure 14b:

$$\begin{aligned} \text{SFR}_{23\mu\text{m}} (M_{\odot}\text{yr}^{-1}) = \\ (1.006 \pm 0.129) \text{SFR}_{\text{FUV}+24\mu\text{m}} (M_{\odot}\text{yr}^{-1}) - (0.05 \pm 0.06), \end{aligned} \quad (19)$$

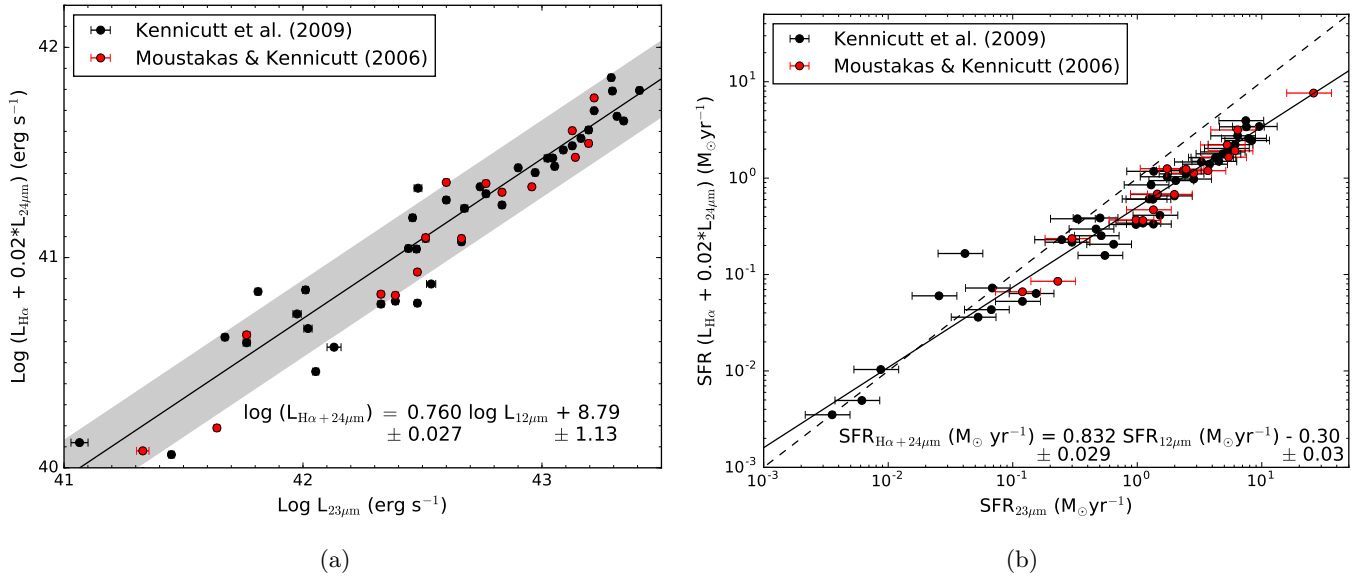


**Figure 11.** Same as Figure 10, but now comparing to  $L_{23\mu\text{m}}$  in (a) and  $23\mu\text{m}$ -derived SFRs (Equation 4) in (b). The linear trend in (a) has a 1- $\sigma$  scatter of 0.18 and indicates a tighter correlation than what was found for  $L_{12\mu\text{m}}$ . Similarly, the SFR relation in (b) has a 1- $\sigma$  scatter of only 0.10 dex. Given that the *WISE*  $23\mu\text{m}$  band is so similar to the MIPS  $24\mu\text{m}$  band, it is probably not surprising and some of the tightness in the relation arises from the x and y axes not being independent. Compared to the one-to-one relation (dashed line) we observe the same trend as in Figure 10b where the *WISE*-derived SFR is systematically high for  $\text{SFR} > 0.1 M_{\odot} \text{ yr}^{-1}$

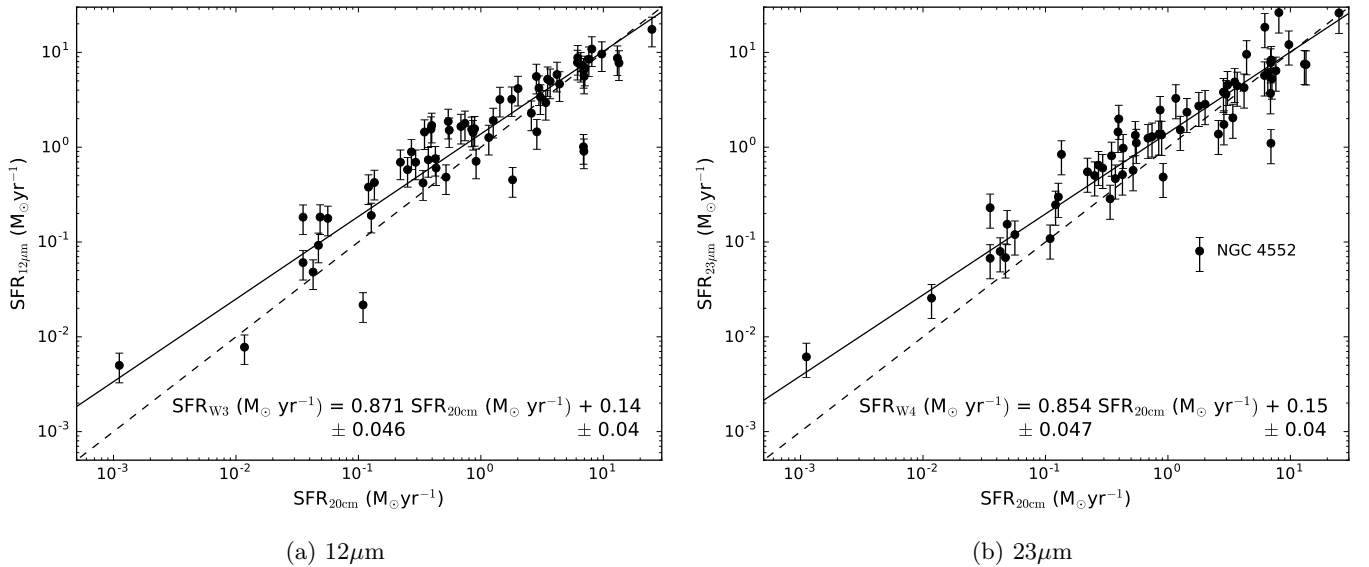


**Figure 12.** Comparison of the *WISE* a)  $12\mu\text{m}$ -derived SFRs and b)  $23\mu\text{m}$ -derived SFRs compared to the radio continuum ( $20\text{cm}$ ) SFRs. The dashed line shows a one-to-one relation, while the solid line is a fit to the points, clearly showing a trend for both the W3 and W4 SFRs to be higher than the  $20\text{cm}$ -derived values. Although the  $23\mu\text{m}$  comparison appears to have fewer outliers compared to the  $12\mu\text{m}$ -derived, the fits are very similar with the  $12\mu\text{m}$  and  $23\mu\text{m}$  relations both having a 1- $\sigma$  scatter of 0.26 dex.

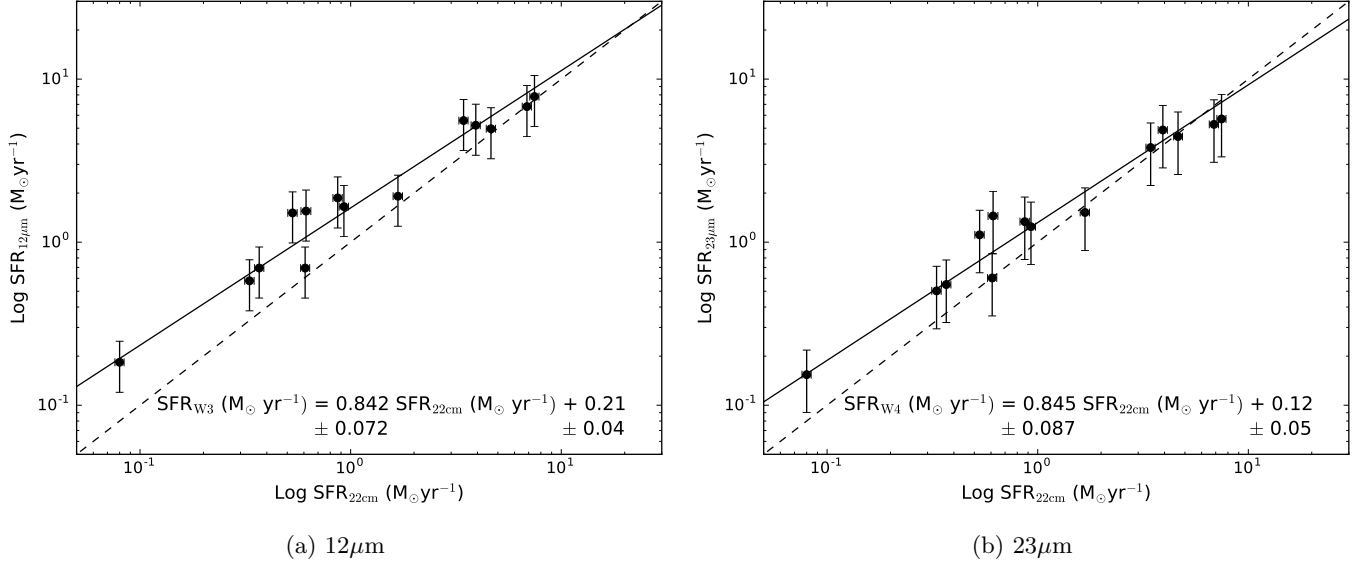


**Figure 13.** Comparison of the *WISE* a) 12 $\mu\text{m}$ -derived SFRs and b) 23 $\mu\text{m}$ -derived SFRs compared to the radio continuum (22 cm) SFRs from Heesen et al. (2014) with a one-to-one relation given by the dashed line. The best linear fit to the data points has a 1- $\sigma$  scatter of  $< 0.001$  for both plots. A similar trend is seen as in Figure 12 where the mid-infrared SFRs tend to be higher than the radio continuum-derived SFRs, particularly at low SFR.

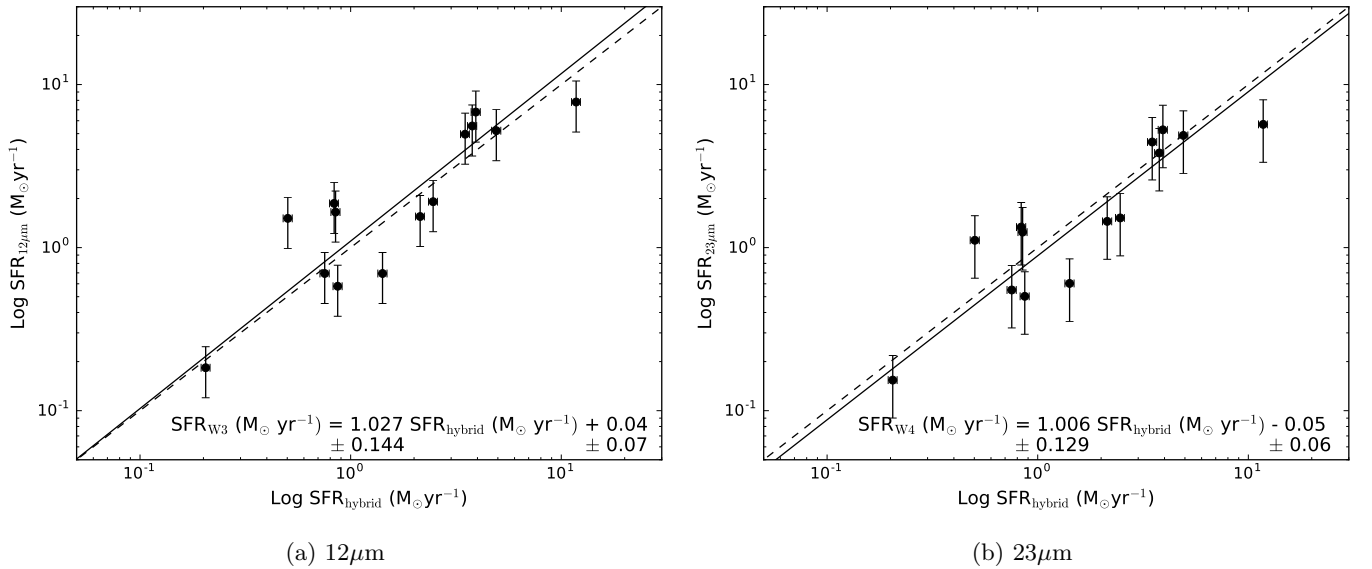


**Figure 14.** Comparison of the *WISE* a) 12 $\mu\text{m}$ -derived SFRs and b) 23 $\mu\text{m}$ -derived SFRs compared to the “hybrid” (FUV+24 $\mu\text{m}$ ) SFRs from Heesen et al. (2014). Both W3- and W4-derived SFRs appear to behave consistently compared to the “hybrid” SFR, appearing to scatter around a one-to-one relation (dashed line). The best fit line in a) has a scatter of 0.19 dex, while b) has a 1- $\sigma$  scatter of 0.11 dex.

with a  $1\text{-}\sigma$  scatter of 0.11 dex.

Considering that in Figure 14a we are using entirely independent methods and tracers to compare SFRs, this result illustrates the utility of W3-derived SFRs, although additional data points would allow for a more substantive comparison.

### 3.5. Specific Star Formation in SINGS/KINGSFISH

Here we use the SFR, derived using the W3 luminosity and Equation (2), in combination with the stellar mass relation of Cluver et al. (2014) to explore star formation in relation to stellar mass in the SINGS/KINGFISH sample.

In Figure 15a we plot SFR as a function of stellar mass, color coding galaxies by their W2–W3 color, and include the “Main Sequence” relations for local galaxies ( $z = 0$ ) from Elbaz et al. (2007) and Bauermeister et al. (2013), who choose their relation to be consistent with that of Bouché et al. (2010), Karim et al. (2011) and Elbaz et al. (2011). We also include the fit from the *Spitzer* Local Volume Legacy (LVL) study (Cook et al. 2014) and the GAMA-G12 study of Jarrett et al. (2017). As we have color-coded by W2–W3 colour, the bluer colors represent low star-forming, spheroidal systems. As indicated by this figure, these systems occupy both the low mass and high mass regions of the diagram: dwarf spheroids lie at the low mass end experiencing relatively low star formation, while elliptical galaxies with high mass and low (quenched) to non-existent star formation, are at the other end. For intermediate W2–W3 color, the LVL relation of Cook et al. (2014) matches the SINGS/KINGFISH most closely, while the other relations do better for the higher star-forming systems, where  $3 < \text{W2} - \text{W3} < 4$ .

An alternative view is presented in Figure 15b where we show specific SFR (sSFR; SFR divided by stellar mass) versus stellar mass, once again color-coded by W2–W3 color. From this diagram we see a clear separation as a function of star formation, where systems with high specific star formation have W2–W3 colors  $> 3$  and stellar masses between  $10^9$  and  $10^{11} M_{\odot}$ . Systems with low specific star formation have W2–W3 colors  $< 1.5$  and typically have masses  $> 10^{11} M_{\odot}$ . An intermediate band appears between  $\log \text{sSFR}$  of -10 and -11, exhibiting a broad range of stellar mass and W2–W3 colors between 1.5 and 3.

## 4. DISCUSSION

The *Spitzer* Space Telescope enabled detailed study of SFR indicators in the mid-infrared and extensively investigated the use of monochromatic tracers of star formation. The MIPS  $24\mu\text{m}$  band measures the warm dust

continuum and is relatively uncontaminated by emission line and aromatic features, similar to the *WISE*  $23\mu\text{m}$  band, and can be related to  $L_{\text{TIR}}$ , and therefore SFR as shown in Rujopakarn et al. (2013). However, this tracer is sensitive to the presence of an AGN, which produces an excess of continuum emission, as well as the dust geometry in relation to the heating source (Farrah et al. 2008).

As shown in Section 3.2, the *WISE* W3 band shows a tighter correlation with  $L_{\text{TIR}}$  SFR in the absence of strong silicate absorption usually associated with embedded starbursts, i.e. coupled to a significant dust column (e.g. local ULIRGs; Desai et al. 2007). Although the center of this band is close to the  $11.3\mu\text{m}$  PAH feature, as discussed in Appendix A, the fractional contribution of the  $11.3\mu\text{m}$  PAH feature is relatively low – the largest contribution being 11.6% for NGC 4559. In terms of total PAH contribution to W3, this varies from 2.9% (NGC 584) to 52.6% (NGC 925).

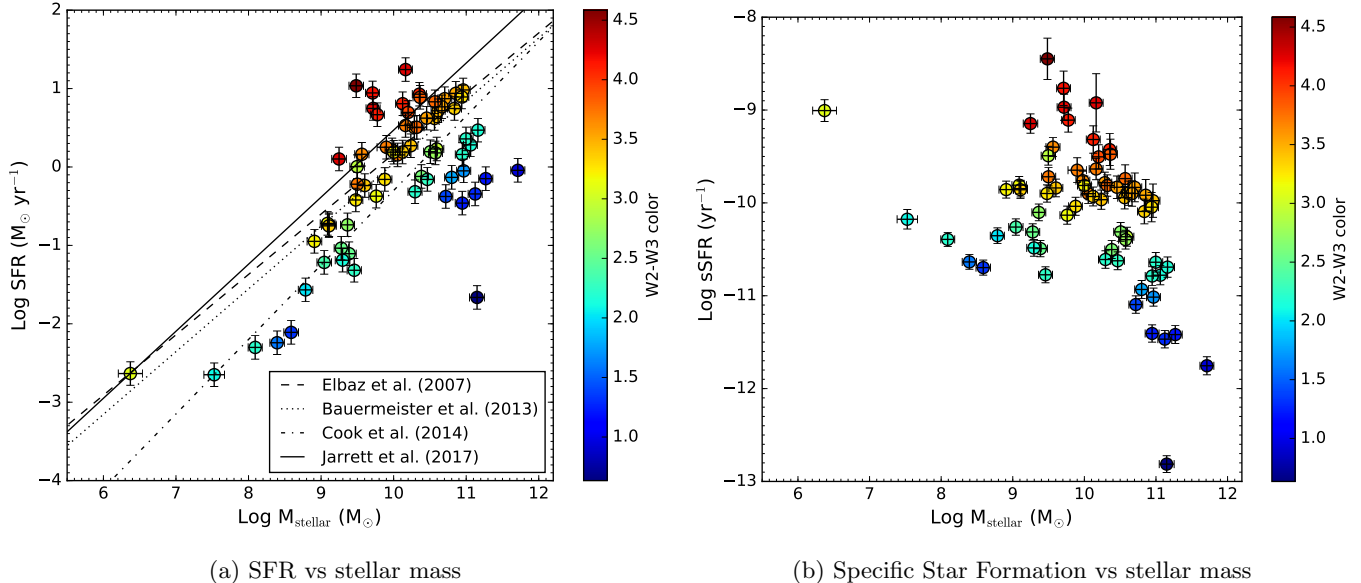
Although PAH features do trace star formation (Förster Schreiber et al. 2004; Houck et al. 2007; Diamond-Stanic & Rieke 2012; Alonso-Herrero et al. 2014; Shipley et al. 2016), hard radiation fields destroy PAHs, and as a result AGN and low metallicity environments significantly suppress PAH emission (Smith et al. 2007). PAH emission varies depending on the physical conditions of a given star-forming region, and is therefore not constant across a galaxy (Smith et al. 2007; Draine & Li 2007).

Figure 4a shows the steady response of the W3 band as  $L_{\text{TIR}}$  increases, yielding a tight correlation (Figure 5) extending to even relatively extreme star-forming systems. Although we do not probe very low metallicity environments in our sample, the lack of influence of metallicity on the W3 SFR relation is consistent with the fact that the  $11.3\mu\text{m}$  PAH feature and combined PAH contribution to the band is ameliorated by the more substantial contributions from the continuum arising from warm, large grains (Appendix A).

The relation between W3 and  $L_{\text{TIR}}$  suggests that W3 must be sampling a range of excitation sources to closely mimic the behaviour of the total infrared emission of the galaxy. The warm, large grains and stochastically heated grains, as well as the PAH features (Li & Draine 2002), will be powered by contributions from both hot and cool stars, similar to  $L_{\text{TIR}}$ . However, we would not expect this relation to hold for sub-regions of a galaxy where variations in dust composition, temperature and PAH characteristics would likely produce large fluctuations.

## 5. CONCLUSIONS





**Figure 15.** Plot of a) log SFR and b) log sSFR vs log stellar mass, using the  $12\mu\text{m}$  SFR calibration given by Equation (2), for the SINGS/KINGFISH sample, color-coded by W2–W3 color. The “Main Sequence” relations from Elbaz et al. (2007), Bauermeister et al. (2013), Cook et al. (2014), and Jarrett et al. (2017), is shown as dashed, dotted, dot-dash, and solid lines, respectively in (a). For  $1.5 < W2-W3 < 3$  the LVL relation of Cook et al. (2014) is most closely matched, while the other relations do better for  $3 < W2-W3 < 4$ .

In this paper we have derived star formation relations that rely exclusively on the  $12\mu\text{m}$  and  $23\mu\text{m}$  bands of *WISE*, calibrated to  $L_{\text{TIR}}$ . The W3 relation in particular shows a tight correlation, that suggests it could be as reliable as  $L_{\text{TIR}}$  as a SFR indicator, over nearly 5 orders of magnitude in star formation and  $12\mu\text{m}$  luminosity, and similarly, stellar mass range,  $10^7 M_{\odot}$  to  $10^{11.5} M_{\odot}$ . For the most extreme infrared-luminous galaxies, the *WISE* W3 and W4 relations may be, respectively, under-estimating and over-estimating the star formation activity.

The W3 band appears to be a reliable SFR measure in the absence of strong silicate absorption common in

compact, dust-embedded starbursts, and powerful AGN. Taking these caveats into consideration, the benefit of using a SFR tracer unaffected by uncertainties due to dust extinction corrections may well be a key consideration for large area surveys in the future.

The tight relationship we have found between  $L_{12\mu\text{m}}$  and  $L_{\text{TIR}}$ , and the known correlation that exists between the mid-infrared  $24\mu\text{m}$  and radio continuum (e.g. Appleton et al. 2004), suggests that the W3 band can be used in combination with upcoming sensitive, large-area radio surveys to disentangle star formation and AGN heating.

## APPENDIX

### A. *WISE* SPECTRAL BANDS

The *WISE* relative system response curves are given in Jarrett et al. (2011), comprising four bands centered on 3.4, 4.6, 12 and  $23\mu\text{m}$  in the infrared window. The first two are essentially the near-infrared, sensitive to the evolved populations in galaxies, while the second two are mid-infrared ISM bands. W3 is notably broad in spectral coverage, as demonstrated in Fig.16, showing the spectral energy distribution (SED) of the SINGS galaxy, NGC 337. As a late-type barred spiral, NGC 337 has active star formation, exhibiting strong molecular (PAHs) and thermal (dust) continuum emission. The W3 band encompasses the  $7.7\mu\text{m}$  and  $8.5\mu\text{m}$  PAH features (typically traced by the IRAC-4 band), the  $10\mu\text{m}$  silicate absorption,  $11.3\mu\text{m}$  PAH band,  $12.8\mu\text{m}$  [Ne II] and  $15.7\mu\text{m}$  [Ne III] nebular emission.

Convoluting SINGS global spectra with the W3 response function and measuring the fractional contribution of the  $11.3\mu\text{m}$  PAH indicates that it only contributes (on average) 7.5% to the W3 flux (J.D.T Smith, private communication). Taking into account all PAH features, this increases to 34%. The contribution from emission lines is 3.5% on average. The W3 band is therefore dominated by non-PAH continuum, coming from warm, large grains and stochastically heated grains.

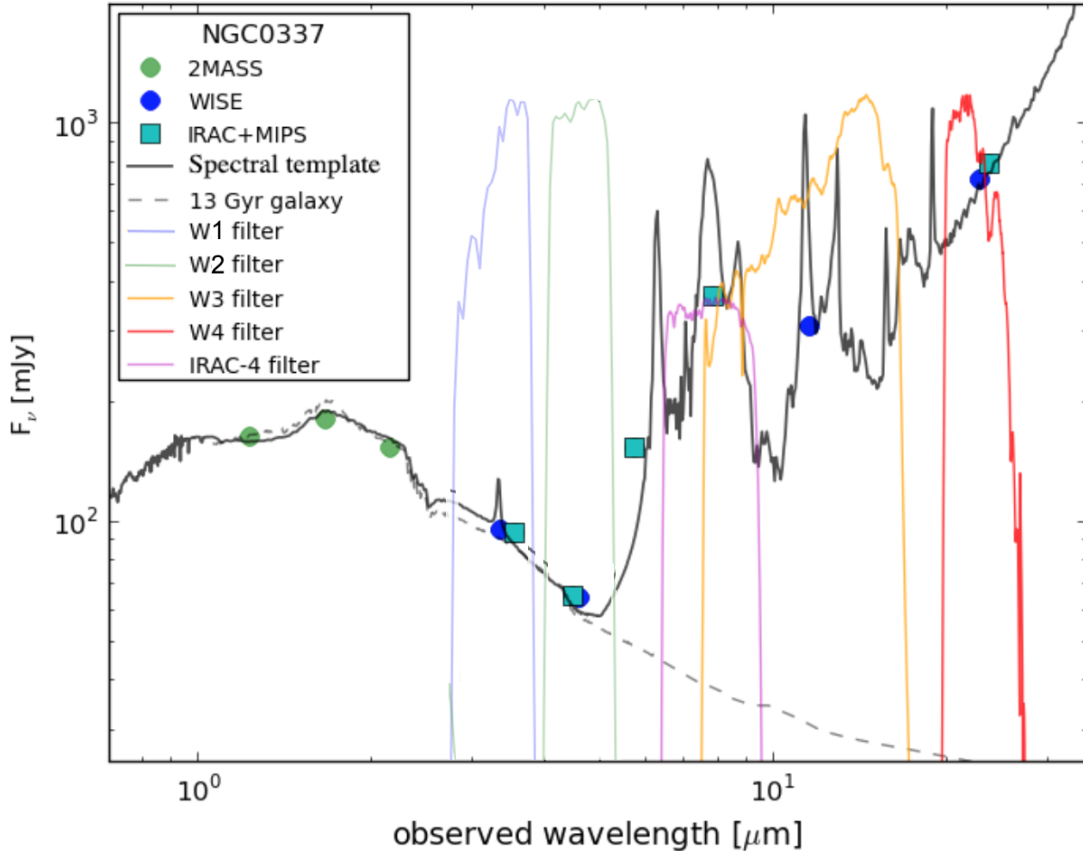


**Figure 16.** Infrared spectral energy distribution for the galaxy NGC 337. The global fluxes come from 2MASS (green), WISE (blue) and Spitzer (cyan). For comparison, two composite templates (Brown et al. 2014a) are shown: late-type that highlights the ISM emission components, and an early-type that isolates the stellar (evolved) component. Note the broad spectral coverage of the *WISE* W3 ( $12\mu\text{m}$ ) band, which overlaps with IRAC-4 ( $8\mu\text{m}$ ) band and extends to nearly  $16\mu\text{m}$ .

For example, NGC 337 (Figure 16), has a fractional contribution of 45.3% from all PAH features, 10.4% from the  $11.3\mu\text{m}$  PAH and 5.0% from the nebular emission lines. The most IR-luminous galaxy in the sample, NGC 7331, has a fractional contribution of 37.4% from all PAH features, 8.5% from the  $11.3\mu\text{m}$  PAH and 2.4% from the nebular emission lines.

The dwarf galaxy NGC 1705 has, in comparison, a fractional contribution of 21.5% from all PAH features, 7.6% from the  $11.3\mu\text{m}$  PAH and 13.3% from the nebular emission lines

We thank the anonymous referee for recommendations that improved the content of this paper. MEC and THJ acknowledge funding from the National Research Foundation under the Research Career Advancement and South African Research Chair Initiative programs, respectively. This publication makes use of data products from the Wide-field Infrared Survey Explorer, which is a joint project of the University of California, Los Angeles, and the Jet Propulsion Laboratory/California Institute of Technology, funded by the National Aeronautics and Space Administration.

This research has made use of the NASA/IPAC Extragalactic Database (NED) which is operated by the Jet Propulsion Laboratory, California Institute of Technology, under contract with the National Aeronautics and Space Administration.

## REFERENCES

- Aalto, S., Costagliola, F., Muller, S., et al. 2016, *A&A*, 590, A73
- Alatalo, K., Blitz, L., Young, L. M., et al. 2011, *ApJ*, 735, 88

- Alonso-Herrero, A., Ramos Almeida, C., Esquej, P., et al. 2014, *MNRAS*, 443, 2766
- Appleton, P. N., Fadda, D. T., Marleau, F. R., et al. 2004, *ApJS*, 154, 147
- Armus, L., Mazzarella, J. M., Evans, A. S., et al. 2009, *PASP*, 121, 559
- Baldry, I. K., & Glazebrook, K. 2003, *ApJ*, 593, 258
- Bauermeister, A., Blitz, L., Bolatto, A., et al. 2013, *ApJ*, 763, 64
- Bigiel, F., Leroy, A., Walter, F., et al. 2008, *AJ*, 136, 2846
- Boquien, M., Kennicutt, R., Calzetti, D., et al. 2016, *A&A*, 591, A6
- Bouché, N., Dekel, A., Genzel, R., et al. 2010, *ApJ*, 718, 1001
- Boselli, A., Fossati, M., Gavazzi, G., et al. 2015, *A&A*, 579, A102
- Braun, R., Oosterloo, T. A., Morganti, R., Klein, U., & Beck, R. 2007, *A&A*, 461, 455
- Bravo-Alfaro, H., Brinks, E., Baker, A. J., Walter, F., & Kunth, D. 2004, *AJ*, 127, 264
- Brown, M.J.I., Moustakas, J., Kennicutt, R., et al. 2017, *ApJ*, 847, 2
- Brown, M. J. I., Moustakas, J., Smith, J.-D. T., et al. 2014, *ApJS*, 212, 18
- Brown, M. J. I., Jarrett, T. H., & Cluver, M. E. 2014, *PASA*, 31, HASH
- Brown, M. J. I., Jannuzi, B. T., Floyd, D. J. E., & Mould, J. R. 2011, *ApJL*, 731, L41
- Buat, V., Donas, J., Milliard, B., & Xu, C. 1999, *A&A*, 352, 371
- Calzetti, D. 2013, *Secular Evolution of Galaxies*, 419
- Calzetti, D., Wu, S.-Y., Hong, S., et al. 2010, *ApJ*, 714, 1256
- Calzetti, D., Kennicutt, R. C., Engelbracht, C. W., et al. 2007, *ApJ*, 666, 870
- Calzetti, D., Bohlin, R. C., Kinney, A. L., Storchi-Bergmann, T., & Heckman, T. M. 1995, *ApJ*, 443, 136
- Cannon, J. M., Walter, F., Bendo, G. J., et al. 2005, *ApJL*, 630, L37
- Cappellari, M., Renzini, A., Greggio, L., et al. 1999, *ApJ*, 519, 117
- Casasola, V., Cassarà, L. P., Bianchi, S., et al. 2017, *A&A*, 605, A18
- Casasola, V., Hunt, L., Combes, F., & García-Burillo, S. 2015, *A&A*, 577, A135
- Catalán-Torrecilla, C., Gil de Paz, A., Castillo-Morales, A., et al. 2015, *A&A*, 584, A87
- Chabrier, G. 2003, *PASP*, 115, 763
- Cluver, M. E., Jarrett, T. H., Hopkins, A. M., et al. 2014, *ApJ*, 782, 90
- Condon, J. J., Cotton, W. D., & Broderick, J. J. 2002, *AJ*, 124, 675
- Condon, J. J., Cotton, W. D., Greisen, E. W., et al. 1998, *AJ*, 115, 1693
- Cook, D. O., Dale, D. A., Johnson, B. D., et al. 2014, *MNRAS*, 445, 899
- Cortese, L. 2012, *A&A*, 543, A132
- Costagliola, F., Herrero-Illana, R., Lohfink, A., et al. 2016, *A&A*, 594, A114
- Cutri, R. M., et al. 2013, *VizieR Online Data Catalog*, 2328,
- da Cunha, E., Charlot, S., & Elbaz, D. 2008, *MNRAS*, 388, 1595
- di Serego Alighieri, S., Bianchi, S., Pappalardo, C., et al. 2013, *A&A*, 552, A8
- Dale, D. A., Cook, D. O., Roussel, H., et al. 2017, *ApJ*, 837, 90
- Dale, D. A., Helou, G., Magdis, G. E., et al. 2014, *ApJ*, 784, 83
- Dale, D. A., & Helou, G. 2002, *ApJ*, 576, 159
- Davies, J. I., Baes, M., Bianchi, S., et al. 2017, *PASP*, 129, 044102
- Davies, L. J. M., Driver, S. P., Robotham, A. S. G., et al. 2016, *MNRAS*, 461, 458
- De Looze, I., Baes, M., Bendo, G. J., Cortese, L., & Fritz, J. 2011, *MNRAS*, 416, 2712
- Desai, V., Armus, L., Spoon, H. W. W., et al. 2007, *ApJ*, 669, 810
- Diamond-Stanic, A. M., & Rieke, G. H. 2012, *ApJ*, 746, 168
- Draine, B. T., & Li, A. 2007, *ApJ*, 657, 810
- Elbaz, D., Dickinson, M., Hwang, H. S., et al. 2011, *A&A*, 533, A119
- Elbaz, D., Daddi, E., Le Borgne, D., et al. 2007, *A&A*, 468, 33
- Farrah, D., Lonsdale, C. J., Weedman, D. W., et al. 2008, *ApJ*, 677, 957-969
- Fischer, J., Sturm, E., González-Alfonso, E., et al. 2010, *A&A*, 518, L41
- Ford, G. P., Gear, W. K., Smith, M. W. L., et al. 2013, *ApJ*, 769, 55
- Förster Schreiber, N. M., Roussel, H., Sauvage, M., & Charmandaris, V. 2004, *A&A*, 419, 501
- Gao, Y., Lo, K. Y., Lee, S.-W., & Lee, T.-H. 2001, *ApJ*, 548, 172
- Goldader, J. D., Joseph, R. D., Doyon, R., & Sanders, D. B. 1995, *ApJ*, 444, 97
- Grootes, M. W., Tuffs, R. J., Popescu, C. C., et al. 2017, *AJ*, 153, 111

- Gürkan, G., Hardcastle, M. J., & Jarvis, M. J. 2014, *MNRAS*, 438, 1149
- Hao, C.-N., Kennicutt, R. C., Johnson, B. D., et al. 2011, *ApJ*, 741, 124
- Heesen, V., Brinks, E., Leroy, A. K., et al. 2014, *AJ*, 147, 103
- Helou, G., Roussel, H., Appleton, P., et al. 2004, *ApJS*, 154, 253
- Houck, J. R., Weedman, D. W., Le Floch, E., & Hao, L. 2007, *ApJ*, 671, 323
- Huang, M.-L., & Kauffmann, G. 2015, *MNRAS*, 450, 1375
- Iglesias-Páramo, J., Vílchez, J. M., Galbany, L., et al. 2013, *A&A*, 553, L7
- Jarrett, T. H., Cluver, M.E., et al. 2017, *ApJsubmitted*
- Jarrett, T. H., Masci, F., Tsai, C. W., et al. 2013, *AJ*, 145, 6
- Jarrett, T. H., Masci, F., Tsai, C. W., et al. 2012, *AJ*, 144, 68
- Jarrett, T. H., Cohen, M., Masci, F., et al. 2011, *ApJ*, 735, 112
- Karim, A., Schinnerer, E., Martínez-Sansigre, A., et al. 2011, *ApJ*, 730, 61
- Kennicutt, R. C., Calzetti, D., Aniano, G., et al. 2011, *PASP*, 123, 1347
- Kennicutt, R. C., Jr., Hao, C.-N., Calzetti, D., et al. 2009, *ApJ*, 703, 1672-1695
- Kennicutt, R. C., Jr., Calzetti, D., Walter, F., et al. 2007, *ApJ*, 671, 333
- Kennicutt, R. C., Jr., Armus, L., Bendo, G., et al. 2003, *PASP*, 115, 928
- Kennicutt, R. C., Jr. 1998, *ARA&A*, 36, 189
- Kessler, M. F., Mueller, T. G., Leech, K., et al. 2003, 'The ISO Handbook', Volume I - Mission & Satellite Overview. Version 2.0 (July, 2003). Series edited by T.G. Mueller, J.A.D.L. Blommaert, and P. Garcia-Lario. ESA SP-1262, ISBN No. 92-9092-968-5, ISSN No. 0379-6566. European Space Agency, 2003.
- Kobulnicky, H. A., & Kewley, L. J. 2004, *ApJ*, 617, 240
- Koribalski, B. S., & López-Sánchez, Á. R. 2009, *MNRAS*, 400, 1749
- Kroupa, P. 2002, *Science*, 295, 82
- Lee, J. C., Hwang, H. S., & Ko, J. 2013, *ApJ*, 774, 62
- Leitherer, C., Schaerer, D., Goldader, J. D., et al. 1999, *ApJS*, 123, 3
- Leroy, A. K., Walter, F., Brinks, E., et al. 2008, *AJ*, 136, 2782
- Li, A., & Draine, B. T. 2002, *ApJ*, 572, 232
- Mainzer, A., Bauer, J., Cutri, R. M., et al. 2014, *ApJ*, 792, 30
- Martin, D. C., Fanson, J., Schiminovich, D., et al. 2005, *ApJL*, 619, L1
- Masci, F. 2013, *Astrophysics Source Code Library*, ascl:1302.010
- Momose, R., Koda, J., Kennicutt, R. C., Jr., et al. 2013, *ApJL*, 772, L13
- Moustakas, J., Kennicutt, R. C., Jr., Tremonti, C. A., et al. 2010, *ApJS*, 190, 233-266
- Moustakas, J., & Kennicutt, R. C., Jr. 2006, *ApJS*, 164, 81
- Murphy, E. J., Condon, J. J., Schinnerer, E., et al. 2011, *ApJ*, 737, 67
- Natale, G., Popescu, C. C., Tuffs, R. J., & Semionov, D. 2014, *MNRAS*, 438, 3137
- Neugebauer, G., Habing, H. J., van Duinen, R., et al. 1984, *ApJL*, 278, L1
- Noll, S., Burgarella, D., Giovannoli, E., et al. 2009, *A&A*, 507, 1793
- Pilbratt, G. L., Riedinger, J. R., Passvogel, T., et al. 2010, *A&A*, 518, L1
- Planck Collaboration, Adam, R., Ade, P. A. R., et al. 2016, *A&A*, 594, A1
- Popescu, C. C., Misiriotis, A., Kylafis, N. D., Tuffs, R. J., & Fischera, J. 2000, *A&A*, 362, 138
- Rahman, N., Bolatto, A. D., Wong, T., et al. 2011, *ApJ*, 730, 72
- Richards, S. N., Bryant, J. J., Croom, S. M., et al. 2016, *MNRAS*, 455, 2826
- Rieke, G. H., Alonso-Herrero, A., Weiner, B. J., et al. 2009, *ApJ*, 692, 556
- Rieke, G. H., Loken, K., Rieke, M. J., & Tamblyn, P. 1993, *ApJ*, 412, 99
- Robotham, A. S. G., & Obreschkow, D. 2015, *PASA*, 32, e033
- Roussel, H., Helou, G., Smith, J. D., et al. 2006, *ApJ*, 646, 841
- Roussel, H., Helou, G., Beck, R., et al. 2003, *ApJ*, 593, 733
- Rujopakarn, W., Rieke, G. H., Weiner, B. J., et al. 2013, *ApJ*, 767, 73
- Sanders, D. B., Mazzarella, J. M., Kim, D.-C., Surace, J. A., & Soifer, B. T. 2003, *AJ*, 126, 1607
- Sandstrom, K. M., Bolatto, A. D., Draine, B. T., Bot, C., & Stanimirović, S. 2010, *ApJ*, 715, 701
- Shapiro, K. L., Falcón-Barroso, J., van de Ven, G., et al. 2010, *MNRAS*, 402, 2140
- Shiple, H. V., Papovich, C., Rieke, G. H., Brown, M. J. I., & Moustakas, J. 2016, *ApJ*, 818, 60
- Silva, L., Granato, G. L., Bressan, A., & Danese, L. 1998, *ApJ*, 509, 103
- Smith, J. D. T., Draine, B. T., Dale, D. A., et al. 2007, *ApJ*, 656, 770
- Stern, D., Assef, R. J., Benford, D. J., et al. 2012, *ApJ*, 753, 30



- Takeuchi, T. T., Buat, V., Iglesias-Páramo, J., Boselli, A., & Burgarella, D. 2005, *A&A*, 432, 423
- Walter, F., Brinks, E., de Blok, W. J. G., et al. 2008, *AJ*, 136, 2563-2647
- Werner, M. W., Roellig, T. L., Low, F. J., et al. 2004, *ApJS*, 154, 1
- Wijesinghe, D. B., da Cunha, E., Hopkins, A. M., et al. 2011, *MNRAS*, 415, 1002
- Wright, E. L., Eisenhardt, P. R. M., Mainzer, A. K., et al. 2010, *AJ*, 140, 1868-1881
- Wu, H., Cao, C., Hao, C.-N., et al. 2005, *ApJL*, 632, L79
- Zhu, Y.-N., Wu, H., Cao, C., & Li, H.-N. 2008, *ApJ*, 686, 155-171

Table 1. Measured *WISE* properties of the SINGS/KINGFISH Sample

Galaxy	W1 (mag)	W1f	W2 (mag)	W2f	W3 (mag)	W3f	W4 (mag)	W4f	Radius (arcsec)	b/a	P.A. (deg.)
NGC0024	8.66 ± 0.011	0	8.682 ± 0.02	0	6.176 ± 0.033	10	4.49 ± 0.06	10	187.97	0.296	45.1
NGC0037	8.777 ± 0.011	0	8.552 ± 0.02	0	4.912 ± 0.017	10	2.549 ± 0.02	10	101.98	0.622	131.8
NGC0584	7.19 ± 0.011	0	7.247 ± 0.019	0	6.781 ± 0.05	10	5.757 ± 0.107	10	190.32	0.784	70.6
NGC0628	6.442 ± 0.011	0	6.332 ± 0.019	0	2.701 ± 0.015	10	0.882 ± 0.018	10	324.47	0.819	86.4
NGC0855	9.665 ± 0.012	0	9.592 ± 0.021	0	7.229 ± 0.07	10	4.976 ± 0.048	10	106.47	0.446	65.0
NGC0925	7.57 ± 0.011	0	7.517 ± 0.02	0	4.243 ± 0.034	10	2.252 ± 0.058	10	311.71	0.501	110.1
NGC1097	5.983 ± 0.011	0	5.882 ± 0.019	0	2.469 ± 0.013	10	0.131 ± 0.014	10	322.65	0.792	112.9
NGC1266	9.385 ± 0.012	0	9.091 ± 0.021	0	6.199 ± 0.018	10	2.557 ± 0.016	10	65.89	0.733	115.4
NGC1291	5.35 ± 0.011	0	5.391 ± 0.019	0	4.156 ± 0.06	10	3.043 ± 0.102	10	431.86	0.987	55.1
NGC1316	5.079 ± 0.011	0	5.102 ± 0.019	0	4.17 ± 0.038	10	2.783 ± 0.047	10	768.93	0.645	34.7
NGC1377	9.507 ± 0.012	0	8.153 ± 0.02	0	4.682 ± 0.014	10	1.712 ± 0.013	10	72.06	0.636	92.0
NGC1404	6.611 ± 0.014	0	6.651 ± 0.023	0	6.021 ± 0.086	10	5.049 ± 0.067	10	216.32	0.88	160.0
NGC1482	7.938 ± 0.011	0	7.629 ± 0.019	0	3.418 ± 0.014	10	0.825 ± 0.014	10	135.91	0.799	112.7
NGC1512	7.245 ± 0.011	0	7.246 ± 0.019	0	4.639 ± 0.027	10	3.005 ± 0.036	10	291.06	0.644	45.3
NGC1566	6.568 ± 0.011	0	6.465 ± 0.019	0	2.956 ± 0.013	10	1.048 ± 0.015	10	333.13	0.735	27.1
NGC1705	10.085 ± 0.012	0	10.001 ± 0.021	0	7.983 ± 0.036	10	5.407 ± 0.064	10	94.69	0.595	44.2
M81DwA	16.989 ± 0.138	1	16.543 ± 0.329	1	- ± -	0	11.362 ± 2.735	0	6.01	1.0	98.8
DDO053	12.598 ± 0.022	0	12.277 ± 0.053	0	9.182 ± 0.077	0	6.324 ± 0.13	10	49.3	0.789	138.5
NGC2403	5.689 ± 0.011	0	5.59 ± 0.019	0	2.203 ± 0.016	10	0.195 ± 0.023	10	656.59	0.528	124.1
NGC2798	8.658 ± 0.011	0	8.384 ± 0.019	0	4.278 ± 0.014	10	1.302 ± 0.013	10	94.13	0.522	158.4
NGC2841	5.89 ± 0.011	0	5.892 ± 0.019	0	3.742 ± 0.014	10	2.038 ± 0.04	10	384.35	0.47	151.4
NGC2915	9.427 ± 0.012	0	9.383 ± 0.021	0	7.783 ± 0.036	10	5.331 ± 0.052	10	123.78	0.493	129.7
NGC2976	7.155 ± 0.011	0	7.055 ± 0.019	0	3.837 ± 0.017	10	1.838 ± 0.017	10	237.09	0.589	144.3
NGC3031	3.606 ± 0.011	0	3.608 ± 0.019	0	1.826 ± 0.012	10	0.426 ± 0.021	10	868.41	0.557	155.9
NGC3049	9.774 ± 0.012	0	9.727 ± 0.022	0	6.027 ± 0.02	10	3.237 ± 0.021	10	78.19	0.624	26.0
M81DwB	12.046 ± 0.017	0	11.96 ± 0.043	0	9.873 ± 0.144	0	7.615 ± 0.405	0	66.28	0.501	139.9
NGC3190	7.298 ± 0.011	0	7.258 ± 0.019	0	5.054 ± 0.019	10	3.64 ± 0.029	10	178.48	0.45	121.1
NGC3184	6.987 ± 0.011	0	6.911 ± 0.019	0	3.508 ± 0.015	10	1.769 ± 0.021	10	227.06	0.934	106.7
NGC3198	7.609 ± 0.011	0	7.52 ± 0.019	0	4.171 ± 0.02	10	2.116 ± 0.025	10	279.97	0.349	35.3
IC2574	8.681 ± 0.012	0	8.592 ± 0.022	0	7.27 ± 0.084	10	4.1 ± 0.108	0	326.09	0.49	39.6
NGC3265	10.216 ± 0.012	0	10.125 ± 0.021	0	6.415 ± 0.016	10	3.67 ± 0.022	10	36.53	0.898	68.9
Mrk33	10.23 ± 0.012	0	10.006 ± 0.022	0	5.74 ± 0.013	10	2.471 ± 0.014	10	56.68	0.784	125.4
NGC3351	6.464 ± 0.011	0	6.459 ± 0.019	0	3.502 ± 0.018	10	1.226 ± 0.016	10	245.14	0.78	17.2
NGC3521	5.439 ± 0.011	0	5.342 ± 0.019	0	1.938 ± 0.014	10	0.276 ± 0.018	10	427.58	0.621	165.4

Table 1 continued

Table 1 (*continued*)

Galaxy	W1 (mag)	W1f	W2 (mag)	W2f	W3 (mag)	W3f	W4 (mag)	W4f	Radius (arcsec)	b/a	P.A. (deg.)
NGC3621	6.38 ± 0.02	0	6.241 ± 0.034	0	2.546 ± 0.014	10	0.775 ± 0.023	10	349.92	0.478	162.4
NGC3627	5.556 ± 0.011	0	5.446 ± 0.019	0	1.997 ± 0.013	10	-0.025 ± 0.015	10	395.56	0.532	177.3
NGC3773	10.464 ± 0.012	0	10.346 ± 0.022	0	7.171 ± 0.03	10	4.45 ± 0.029	10	55.96	0.834	173.7
NGC3938	7.496 ± 0.011	0	7.371 ± 0.019	0	3.816 ± 0.016	10	2.057 ± 0.019	10	182.74	0.823	49.5
NGC4125	6.501 ± 0.011	0	6.535 ± 0.019	0	6.089 ± 0.052	10	5.014 ± 0.067	10	336.66	0.71	83.9
NGC4236	7.91 ± 0.011	0	7.99 ± 0.02	0	5.749 ± 0.087	10	3.091 ± 0.047	0	519.32	0.299	158.0
NGC4254	6.65 ± 0.011	0	6.464 ± 0.019	0	2.375 ± 0.013	10	0.6 ± 0.014	10	174.03	0.926	58.3
NGC4321	6.247 ± 0.011	0	6.122 ± 0.019	0	2.578 ± 0.015	10	0.722 ± 0.02	10	322.35	0.889	55.2
NGC4450	6.883 ± 0.011	0	6.892 ± 0.019	0	5.198 ± 0.028	10	3.693 ± 0.063	10	216.86	0.674	172.3
NGC4536	7.183 ± 0.011	0	7.027 ± 0.019	0	3.332 ± 0.016	10	0.866 ± 0.016	10	262.54	0.388	122.9
NGC4552	6.359 ± 0.011	0	6.425 ± 0.019	0	5.134 ± 0.124	10	4.856 ± 0.166	10	321.51	0.882	134.4
NGC4559	7.389 ± 0.011	0	7.235 ± 0.019	0	4.037 ± 0.018	10	2.063 ± 0.034	10	297.59	0.379	149.5
NGC4569	6.49 ± 0.011	0	6.427 ± 0.019	0	3.746 ± 0.014	10	1.845 ± 0.015	10	323.95	0.404	25.3
NGC4579	6.325 ± 0.011	0	6.29 ± 0.019	0	4.133 ± 0.014	10	2.584 ± 0.021	10	242.89	0.794	97.4
NGC4594	4.617 ± 0.011	0	4.639 ± 0.019	0	3.439 ± 0.036	10	2.248 ± 0.04	10	660.83	0.455	90.7
NGC4625	9.592 ± 0.012	0	9.517 ± 0.021	0	6.152 ± 0.024	10	4.404 ± 0.061	10	64.37	0.9	177.5
NGC4631	6.005 ± 0.011	0	5.802 ± 0.019	0	1.959 ± 0.013	10	-0.1 ± 0.014	10	496.31	0.272	83.2
NGC4725	6.086 ± 0.011	0	6.106 ± 0.019	0	3.891 ± 0.021	10	2.54 ± 0.026	10	386.33	0.634	40.0
NGC4736	4.767 ± 0.011	0	4.742 ± 0.019	0	1.992 ± 0.015	10	0.27 ± 0.02	10	579.39	0.89	105.6
DDO154	12.334 ± 0.022	0	12.533 ± 0.077	0	11.19 ± 0.591	0	- ± -	0	60.6	0.575	39.5
NGC4826	5.183 ± 0.011	0	5.169 ± 0.019	0	2.911 ± 0.016	10	1.15 ± 0.018	10	369.88	0.535	114.7
DDO165	11.125 ± 0.014	0	11.143 ± 0.035	0	- ± -	0	8.729 ± 1.558	0	114.65	0.521	98.2
NGC5033	6.719 ± 0.011	0	6.618 ± 0.019	0	3.086 ± 0.014	10	1.365 ± 0.028	10	283.42	0.574	172.5
NGC5055	5.257 ± 0.011	0	5.195 ± 0.019	0	1.85 ± 0.013	10	0.204 ± 0.016	10	523.49	0.601	103.4
NGC5194	5.087 ± 0.011	0	4.968 ± 0.019	0	1.176 ± 0.012	10	-0.638 ± 0.014	10	463.09	0.666	17.6
NGC5195	6.451 ± 0.011	0	6.432 ± 0.019	0	4.223 ± 0.012	10	2.009 ± 0.013	10	174.12	0.776	106.9
NGC5408	10.006 ± 0.012	0	9.915 ± 0.022	0	6.714 ± 0.022	0	3.233 ± 0.021	10	83.72	0.601	60.5
NGC5474	8.646 ± 0.011	0	8.609 ± 0.02	0	6.083 ± 0.051	10	4.28 ± 0.086	10	155.1	0.85	1.1
NGC5713	7.966 ± 0.011	0	7.75 ± 0.019	0	3.656 ± 0.013	10	1.31 ± 0.013	10	112.14	0.883	9.2
NGC5866	6.62 ± 0.011	0	6.603 ± 0.019	0	5.205 ± 0.019	10	3.864 ± 0.036	10	283.19	0.555	122.3
IC4710	9.369 ± 0.012	0	9.333 ± 0.022	0	7.194 ± 0.037	0	4.815 ± 0.083	0	130.61	0.75	115.1
NGC6822	5.85 ± 0.011	0	5.843 ± 0.019	0	3.621 ± 0.086	10	1.203 ± 0.092	10	545.48	0.789	136.9
NGC6946	5.015 ± 0.011	0	4.839 ± 0.019	0	0.928 ± 0.011	10	-1.066 ± 0.012	10	446.82	0.909	51.5
NGC7331	5.702 ± 0.011	0	5.61 ± 0.019	0	2.329 ± 0.012	10	0.627 ± 0.015	10	373.35	0.426	172.0
NGC7552	7.132 ± 0.011	0	6.733 ± 0.019	0	2.577 ± 0.013	10	-0.408 ± 0.012	10	152.04	0.8	104.8
NGC7793	6.518 ± 0.011	0	6.428 ± 0.019	0	3.171 ± 0.014	10	1.492 ± 0.018	10	336.27	0.617	97.9

Table 1 *continued*

Table 1 (*continued*)

Galaxy	W1 (mag)	W1f	W2 (mag)	W2f	W3 (mag)	W3f	W4 (mag)	W4f	Radius (arcsec)	b/a	P.A. (deg.)
IC0342	3.974 ± 0.012	0	3.892 ± 0.02	0	0.107 ± 0.034	10	-1.833 ± 0.012	10	778.51	0.946	75.5
M101	5.215 ± 0.011	0	5.1 ± 0.019	0	1.557 ± 0.017	10	-0.384 ± 0.024	10	870.2	0.924	33.3
NGC5398	9.772 ± 0.012	0	9.744 ± 0.022	0	6.598 ± 0.025	10	3.644 ± 0.031	10	101.89	0.642	178.4
NGC3077	6.797 ± 0.011	0	6.706 ± 0.019	0	4.002 ± 0.024	10	1.58 ± 0.02	10	351.94	0.734	38.5
NGC2146	6.383 ± 0.011	0	6.041 ± 0.019	0	1.781 ± 0.014	10	-0.778 ± 0.011	10	250.61	0.552	126.2
NGC3034	4.066 ± 0.012	0	3.611 ± 0.021	0	-0.973 ± 0.011	10	-4.142 ± 0.011	10	363.32	0.787	54.1

NOTE—Integrated fluxes. The flag for each band indicates if the measurement was from: (0)  $1 - \sigma$  isophotal aperture of semi-major axis "Radius", axis ratio and position angle, or (10) the total flux combining the isophotal with the radial SB extrapolation, or (1) the point source measurement from the ALLWISE catalogue.



Table 2. Derived *WISE* properties of the SINGS/KINGFISH Sample

Galaxy	$L_{\text{TR}} \text{ (Wm}^{-2}\text{)}$	$D_{\text{lum}}$ (Mpc)	$W_{3\text{PAH}}$ (mJy)	$W_{4\text{dust}}$ (mJy)	$W_1 - W_2$ (mag)	$W_2 - W_3$ (mag)	$\log L_{W_1}$	$\log L_{W_2}$	$\log L_{W_3}$	$\log L_{W_4}$	$\log L_{W_{1\text{Sun}}}$
NGC0024	-12.5666	6.9	79.4136	116.7656	-0.023	2.507	8.1386 ± 0.010	7.7329 ± 0.012	7.4851 ± 0.024	7.3575 ± 0.026	9.4979 ± 0.014
NGC0337	-12.0051	18.52	293.9644	738.5792	0.228	3.639	8.9513 ± 0.010	8.6461 ± 0.012	8.9112 ± 0.012	9.0164 ± 0.012	10.3106 ± 0.014
NGC0584	-13.3539	20.37	-	14.5342	-0.059	0.469	9.6692 ± 0.010	9.2491 ± 0.012	- ± -	7.3931 ± 0.149	11.0286 ± 0.014
NGC0628	-11.3481	7.23	2227.4197	3362.2595	0.109	3.633	9.0668 ± 0.010	8.7139 ± 0.012	8.9741 ± 0.012	8.8579 ± 0.011	10.4262 ± 0.014
NGC0855	-12.8997	9.74	29.8283	76.437	0.072	2.364	8.0365 ± 0.010	7.6688 ± 0.012	7.3598 ± 0.035	7.4735 ± 0.021	9.3959 ± 0.014
NGC0925	-11.7646	9.16	523.5233	949.6427	0.052	3.275	8.8208 ± 0.010	8.445 ± 0.012	8.5503 ± 0.018	8.514 ± 0.025	10.1801 ± 0.014
NGC1097	-11.1533	17.55	2738.437	6841.18	0.1	3.415	10.0233 ± 0.010	9.6667 ± 0.012	9.8339 ± 0.012	9.9366 ± 0.010	11.3826 ± 0.014
NGC1266	-12.0784	27.91	86.0285	741.4937	0.296	2.905	9.059 ± 0.010	8.781 ± 0.012	8.7339 ± 0.014	9.3744 ± 0.011	10.4183 ± 0.014
NGC1291	-12.0395	8.61	270.7171	336.6199	-0.04	1.235	9.6552 ± 0.010	9.2428 ± 0.012	8.2108 ± 0.114	8.0104 ± 0.053	11.0145 ± 0.014
NGC1316	-12.2435	18.89	166.0631	430.4736	-0.029	0.939	10.4484 ± 0.010	10.0405 ± 0.012	8.6807 ± 0.235	8.7994 ± 0.040	11.8077 ± 0.014
NGC1377	-12.1891	23.35	374.3989	1610.5756	1.363	3.462	8.8622 ± 0.010	9.0109 ± 0.012	9.2179 ± 0.010	9.5565 ± 0.010	10.2215 ± 0.014
NGC1404	-13.5278	19.19	2.4194	33.2088	-0.044	0.634	9.8486 ± 0.010	9.4344 ± 0.013	6.8576 ± 0.500	7.7001 ± 0.100	11.208 ± 0.014
NGC1482	-11.5645	19.61	1191.4984	3640.1294	0.319	4.202	9.3376 ± 0.010	9.0686 ± 0.012	9.5688 ± 0.011	9.7588 ± 0.010	10.6969 ± 0.014
NGC1512	-12.0965	12.01	336.0567	463.3411	-0.002	2.609	9.188 ± 0.010	8.7906 ± 0.012	8.5932 ± 0.021	8.4377 ± 0.017	10.5473 ± 0.014
NGC1566	-11.3787	20.7	1759.6826	2928.889	0.104	3.512	9.9314 ± 0.010	9.5766 ± 0.012	9.7853 ± 0.012	9.7116 ± 0.011	11.2907 ± 0.014
NGC1705	-13.0695	9.12	13.7508	51.2158	0.084	2.02	7.8104 ± 0.010	7.4475 ± 0.012	6.9658 ± 0.033	7.2419 ± 0.027	9.1697 ± 0.014
M81DwA	-13.9309	3.55	-	-	-	-	4.241 ± 0.056	4.0229 ± 0.132	- ± -	- ± -	5.6004 ± 0.057
DDO053	-13.6254	3.55	5.7238	23.0834	0.321	3.095	5.9974 ± 0.012	5.7294 ± 0.023	5.7655 ± 0.033	6.0761 ± 0.053	7.3568 ± 0.016
NGC2403	-11.0229	3.17	3559.5686	6480.167	0.099	3.387	8.6642 ± 0.010	8.3073 ± 0.012	8.4624 ± 0.013	8.4276 ± 0.013	10.0236 ± 0.014
NGC2798	-11.7634	26.39	535.0079	2340.4434	0.282	4.107	9.3021 ± 0.010	9.0184 ± 0.012	9.479 ± 0.011	9.825 ± 0.010	10.6615 ± 0.014
NGC2841	-11.689	14.06	694.688	1106.7286	-0.002	2.152	9.8663 ± 0.010	9.469 ± 0.012	9.0458 ± 0.028	8.9531 ± 0.019	11.2256 ± 0.014
NGC2915	-13.0286	3.76	14.0903	54.9298	0.044	1.6	7.3165 ± 0.010	6.9376 ± 0.012	6.2074 ± 0.054	6.5033 ± 0.023	8.6758 ± 0.014
NGC2976	-11.7055	3.55	780.672	1423.0991	0.1	3.218	8.1747 ± 0.010	7.8182 ± 0.012	7.9003 ± 0.013	7.8661 ± 0.011	9.534 ± 0.014
NGC3031	-10.9432	3.59	3637.6533	4656.822	-0.002	1.782	9.6053 ± 0.010	9.208 ± 0.012	8.5797 ± 0.044	8.392 ± 0.017	10.9646 ± 0.014
NGC3049	-12.5271	30.77	104.157	391.8682	0.049	3.706	8.9893 ± 0.010	8.6125 ± 0.012	8.9019 ± 0.013	9.1824 ± 0.012	10.3487 ± 0.014
M81DwB	-14.0797	5.31	2.4606	-99.0	0.086	2.089	6.556 ± 0.011	6.1939 ± 0.019	5.7485 ± 0.064	- ± -	7.9153 ± 0.015
NGC3190	-12.2179	28.12	211.8346	248.0571	0.037	2.212	9.9017 ± 0.010	9.5198 ± 0.012	9.1317 ± 0.026	8.9053 ± 0.016	11.261 ± 0.014
NGC3184	-11.5971	11.29	1048.2959	1489.8738	0.075	3.406	9.2379 ± 0.010	8.8714 ± 0.012	9.034 ± 0.012	8.8917 ± 0.012	10.5972 ± 0.014
NGC3198	-11.8235	13.81	568.9117	1088.1012	0.091	3.352	9.1635 ± 0.010	8.8035 ± 0.012	8.9434 ± 0.014	8.93 ± 0.013	10.5228 ± 0.014
IC2574	-12.3258	3.8	19.4162	174.1573	0.089	1.322	7.6244 ± 0.010	7.2635 ± 0.012	6.3561 ± 0.082	7.0139 ± 0.044	8.9837 ± 0.014
NGC3265	-12.6741	22.6	73.4912	264.3272	0.094	3.71	8.5486 ± 0.010	8.1899 ± 0.012	8.4821 ± 0.012	8.743 ± 0.012	9.908 ± 0.014
Mark33	-12.3931	24.91	138.9836	815.8638	0.223	4.268	8.6247 ± 0.010	8.3174 ± 0.012	8.8436 ± 0.010	9.3173 ± 0.010	9.984 ± 0.014
NGC3351	-11.5837	10.92	1007.0319	2460.0928	0.005	2.959	9.4176 ± 0.010	9.0231 ± 0.012	8.9871 ± 0.016	9.08 ± 0.011	10.777 ± 0.014
NGC3521	-11.0981	8.61	4429.864	5838.9404	0.097	3.404	9.6201 ± 0.010	9.2624 ± 0.012	9.4247 ± 0.012	9.2496 ± 0.011	10.9794 ± 0.014

Table 2 continued

Table 2 (continued)

Galaxy	$L_{\text{TIR}}$ ( $\text{Wm}^{-2}$ )	$D_{\text{lum}}$ (Mpc)	$W_{3\text{PAH}}$ (mJy)	$W_{4\text{dust}}$ (mJy)	$W1-W2$ (mag)	$W2-W3$ (mag)	$\log L_{W1}$	$\log L_{W2}$	$\log L_{W3}$	$\log L_{W4}$	$\log L_{W1,\text{Sun}}$
NGC3621	-11.2383	7.02	2578.5344	3712.6533	0.14	3.695	9.0657 ± 0.012	8.7252 ± 0.016	9.0121 ± 0.011	8.8755 ± 0.013	10.425 ± 0.015
NGC3627	-11.0106	10.04	4211.5283	7762.558	0.111	3.449	9.7056 ± 0.010	9.3536 ± 0.012	9.5355 ± 0.012	9.5061 ± 0.011	11.0649 ± 0.014
NGC3773	-12.8598	17.0	35.5029	128.0237	0.119	3.178	8.2024 ± 0.010	7.8535 ± 0.012	7.9191 ± 0.017	8.1811 ± 0.014	9.5617 ± 0.014
NGC3938	-11.7086	17.46	799.0945	1150.3269	0.125	3.556	9.4134 ± 0.010	9.0669 ± 0.012	9.2948 ± 0.012	9.158 ± 0.012	10.7727 ± 0.014
NGC4125	-13.0226	21.96	-99.0	31.459	-0.037	0.452	10.01 ± 0.010	9.5986 ± 0.012	- ± -	7.794 ± 0.128	11.3693 ± 0.014
NGC4236	-12.1201	4.47	109.2715	435.3659	-0.081	2.242	8.062 ± 0.010	7.6331 ± 0.012	7.2471 ± 0.044	7.5525 ± 0.021	9.4213 ± 0.014
NGC4254	-11.2238	15.41	3089.4766	4435.8027	0.188	4.088	9.6428 ± 0.010	9.3216 ± 0.012	9.7731 ± 0.010	9.6352 ± 0.010	11.0022 ± 0.014
NGC4321	-11.2668	15.91	2497.652	3942.605	0.125	3.545	9.8321 ± 0.010	9.4856 ± 0.012	9.7088 ± 0.012	9.6121 ± 0.012	11.1914 ± 0.014
NGC4450	-12.2443	19.48	153.4864	226.3166	-0.009	1.7	9.7531 ± 0.010	9.353 ± 0.012	8.6732 ± 0.050	8.5468 ± 0.029	11.1124 ± 0.014
NGC4536	-11.5026	14.4	1257.544	3471.5278	0.156	3.695	9.371 ± 0.010	9.0369 ± 0.012	9.3241 ± 0.012	9.4701 ± 0.011	10.7303 ± 0.014
NGC4552	-13.1491	15.45	113.8553	36.8238	-0.068	1.291	9.7616 ± 0.010	9.3378 ± 0.012	8.342 ± 0.116	7.5568 ± 0.139	11.1209 ± 0.014
NGC4559	-11.6776	13.01	637.4404	1138.5181	0.153	3.2	9.2003 ± 0.010	8.8649 ± 0.012	8.9411 ± 0.013	8.8981 ± 0.016	10.5596 ± 0.014
NGC4569	-11.77	11.84	782.2782	1367.6968	0.063	2.683	9.4776 ± 0.010	9.1063 ± 0.012	8.9478 ± 0.017	8.8955 ± 0.011	10.837 ± 0.014
NGC4579	-11.8328	21.29	493.3753	665.5659	0.032	2.166	10.0534 ± 0.010	9.6695 ± 0.012	9.2574 ± 0.027	9.0924 ± 0.014	11.4127 ± 0.014
NGC4594	-11.8567	9.37	513.3752	714.6739	-0.023	1.201	10.0217 ± 0.010	9.616 ± 0.012	8.5616 ± 0.117	8.4103 ± 0.036	11.381 ± 0.014
NGC4625	-12.6767	10.21	90.8875	130.5536	0.074	3.365	8.1063 ± 0.010	7.7393 ± 0.012	7.8842 ± 0.015	7.7465 ± 0.026	9.4656 ± 0.014
NGC4631	-10.8964	12.13	4491.2637	8430.112	0.204	3.843	9.693 ± 0.010	9.3781 ± 0.012	9.7282 ± 0.011	9.7067 ± 0.010	11.0523 ± 0.014
NGC4725	-11.7135	12.76	614.6294	676.2189	-0.021	2.218	9.7045 ± 0.010	9.2995 ± 0.012	8.9083 ± 0.028	8.6548 ± 0.016	11.0638 ± 0.014
NGC4736	-11.0764	5.18	3926.9233	5776.309	0.024	2.751	9.4472 ± 0.010	9.0603 ± 0.012	8.9307 ± 0.017	8.8033 ± 0.012	10.8066 ± 0.014
DDO154	-14.0824	4.09	-	-	-0.199	-	6.2274 ± 0.012	5.7513 ± 0.032	- ± -	- ± -	7.5868 ± 0.016
NGC4826	-11.3643	5.35	1535.1316	2516.038	0.013	2.259	9.3085 ± 0.010	8.9172 ± 0.012	8.5505 ± 0.025	8.4701 ± 0.012	10.6678 ± 0.014
DDO165	-13.9786	1.55	-	-	-0.018	-	5.865 ± 0.010	5.4613 ± 0.016	- ± -	- ± -	7.2243 ± 0.014
NGC5033	-11.448	17.59	1561.0349	2173.0088	0.1	3.533	9.7308 ± 0.010	9.3743 ± 0.012	9.5918 ± 0.012	9.4405 ± 0.014	11.0902 ± 0.014
NGC5055	-10.9888	9.79	4772.666	6225.7417	0.061	3.346	9.8037 ± 0.010	9.4315 ± 0.012	9.5679 ± 0.012	9.3883 ± 0.011	11.163 ± 0.014
NGC5194	-10.7154	7.9	9139.244	13661.376	0.12	3.792	9.6852 ± 0.010	9.3368 ± 0.012	9.664 ± 0.011	9.5436 ± 0.010	11.0445 ± 0.014
NGC5195	-12.0357	8.03	454.2555	1161.9993	0.019	2.211	9.1533 ± 0.010	8.7644 ± 0.012	8.3741 ± 0.026	8.487 ± 0.011	10.5126 ± 0.014
NGC5408	-12.5801	10.29	53.6192	390.1243	0.09	3.202	7.9475 ± 0.010	7.5869 ± 0.012	7.6618 ± 0.015	8.2287 ± 0.012	9.3068 ± 0.014
NGC5474	-12.4337	7.19	87.7675	143.0601	0.036	2.527	8.1801 ± 0.010	7.798 ± 0.012	7.5645 ± 0.028	7.4817 ± 0.036	9.5395 ± 0.014
NGC5713	-11.657	23.82	943.7425	2313.0437	0.219	4.093	9.4912 ± 0.010	9.1825 ± 0.012	9.6364 ± 0.010	9.7308 ± 0.010	10.8505 ± 0.014
NGC5866	-12.1189	13.98	127.8423	179.8714	0.016	1.4	9.57 ± 0.010	9.1798 ± 0.012	8.3055 ± 0.074	8.1588 ± 0.026	10.9293 ± 0.014
IC4710	-12.7262	10.25	29.0319	88.0063	0.036	2.141	8.1982 ± 0.010	7.8162 ± 0.012	7.3918 ± 0.031	7.5784 ± 0.034	9.5576 ± 0.014
NGC6822	-11.2063	0.46	810.8865	2515.6265	0.007	2.222	6.9202 ± 0.010	6.5265 ± 0.012	6.1404 ± 0.043	6.3371 ± 0.038	8.2796 ± 0.014
NGC6946	-10.637	5.89	11566.118	20351.254	0.177	3.909	9.4601 ± 0.010	9.1344 ± 0.012	9.5114 ± 0.010	9.4619 ± 0.010	10.8194 ± 0.014
NGC7331	-11.0996	14.73	3081.586	4271.3247	0.092	3.282	9.9833 ± 0.010	9.6236 ± 0.012	9.7333 ± 0.012	9.5801 ± 0.011	11.3426 ± 0.014
NGC7552	-11.1823	17.17	2592.8818	11332.939	0.403	4.156	9.5443 ± 0.010	9.3091 ± 0.012	9.7912 ± 0.010	10.1368 ± 0.010	10.9036 ± 0.014
NGC7793	-11.3849	3.93	1444.9513	1946.5873	0.09	3.257	8.5175 ± 0.010	8.157 ± 0.012	8.2557 ± 0.013	8.0902 ± 0.012	9.8768 ± 0.014

Table 2 continued

Table 2 (*continued*)

Galaxy	$L_{\text{TIR}}$ ( $\text{Wm}^{-2}$ )	$D_{\text{lum}}$ (Mpc)	$W_{3\text{FAH}}$ (mJy)	$W_{4\text{dust}}$ (mJy)	$W1-W2$ (mag)	$W2-W3$ (mag)	$\log L_{W1}$	$\log L_{W2}$	$\log L_{W3}$	$\log L_{W4}$	$\log L_{W1\text{Sun}}$
IC0342	-10.3843	3.13	25064.812	42112.3	0.082	3.785	9.3383 ± 0.010	8.9746 ± 0.012	9.2982 ± 0.017	9.2285 ± 0.010	10.6976 ± 0.014
M101	-10.8026	7.23	6359.7734	10806.792	0.115	3.544	9.5576 ± 0.010	9.2071 ± 0.012	9.4297 ± 0.012	9.365 ± 0.013	10.917 ± 0.014
NGC5398	-12.6836	20.57	59.6415	270.3057	0.029	3.152	8.6444 ± 0.010	8.2596 ± 0.012	8.3101 ± 0.016	8.6714 ± 0.015	10.0038 ± 0.014
NGC3077	-11.8005	3.93	634.8691	1801.7534	0.091	2.704	8.4059 ± 0.010	8.0458 ± 0.012	7.8986 ± 0.018	8.0566 ± 0.012	9.7652 ± 0.014
NGC2146	-10.9088	17.51	5397.2617	15935.869	0.349	4.253	9.862 ± 0.010	9.6049 ± 0.012	10.1264 ± 0.011	10.3016 ± 0.010	11.2213 ± 0.014
NGC3034	-9.8625	3.72	70021.49	356701.1	0.455	4.584	9.4509 ± 0.010	9.2364 ± 0.012	9.8937 ± 0.010	10.3058 ± 0.010	10.8102 ± 0.014

Table 3. Measured *WISE* properties of (U)LIRG Sample

Galaxy	W1 (mag)	W1f (-)	W2 (mag)	W2f (-)	W3 (mag)	W3f (-)	W4 (mag)	W4f (-)	Radius	b/a	P.A.
Mrk231	7.498 ± 0.011	0	6.341 ± 0.019	0	3.131 ± 0.012	10	0.04 ± 0.012	10	87.57	1.0	0.6
IRAS17208-0014	10.647 ± 0.012	0	10.011 ± 0.021	0	5.785 ± 0.014	10	2.366 ± 0.027	0	34.31	1.0	174.4
Arp220	9.39 ± 0.011	0	8.941 ± 0.019	0	4.411 ± 0.018	10	0.367 ± 0.013	10	85.48	1.0	5.4
NGC6240	8.721 ± 0.011	0	8.231 ± 0.019	0	4.652 ± 0.018	10	1.125 ± 0.013	10	88.24	0.678	20.9
NGC0695	9.669 ± 0.011	0	9.305 ± 0.019	0	4.899 ± 0.013	10	2.664 ± 0.013	10	45.05	0.861	14.2
Mrk331	9.503 ± 0.011	0	9.103 ± 0.019	0	4.74 ± 0.012	10	1.595 ± 0.012	10	43.66	0.775	150.2
UGC12815	8.004 ± 0.011	0	7.828 ± 0.019	0	4.233 ± 0.023	10	1.856 ± 0.019	10	221.62	0.35	65.7
HPASSJ1004-06	9.017 ± 0.011	0	8.74 ± 0.019	0	4.435 ± 0.027	10	2.175 ± 0.016	10	73.77	0.77	165.5
NGC2388	9.211 ± 0.011	0	8.893 ± 0.019	0	4.68 ± 0.015	10	1.719 ± 0.013	10	50.18	0.871	47.7
NGC2146	6.383 ± 0.011	0	6.041 ± 0.019	0	1.814 ± 0.014	10	-0.779 ± 0.011	10	250.61	0.552	126.2
NGC1365	6.034 ± 0.011	0	5.74 ± 0.019	0	2.112 ± 0.011	10	-0.457 ± 0.011	10	393.3	0.602	39.4
NGC4039	6.915 ± 0.011	0	6.749 ± 0.019	0	2.921 ± 0.014	10	0.299 ± 0.014	10	159.24	0.899	168.3
UGC89	8.568 ± 0.011	0	8.436 ± 0.019	0	4.786 ± 0.015	10	2.347 ± 0.014	10	100.03	0.647	169.3
NGC6701	8.87 ± 0.011	0	8.68 ± 0.019	0	4.667 ± 0.012	10	2.179 ± 0.013	10	70.72	0.978	118.7
UGC1845	9.476 ± 0.011	0	9.173 ± 0.019	0	5.203 ± 0.013	10	2.541 ± 0.013	10	53.24	0.653	129.1
NGC5936	9.04 ± 0.011	0	8.823 ± 0.019	0	4.68 ± 0.012	10	2.188 ± 0.013	10	71.02	0.95	76.5
MCG+02-20-003	10.347 ± 0.012	0	9.294 ± 0.02	0	5.757 ± 0.013	10	2.948 ± 0.014	10	40.16	0.657	152.6
HPASSJ0716-62	8.157 ± 0.011	0	7.925 ± 0.019	0	4.18 ± 0.012	10	1.569 ± 0.012	10	130.24	0.489	177.5
ESO320-G030	8.796 ± 0.011	0	8.581 ± 0.019	0	4.6 ± 0.013	10	1.74 ± 0.012	10	95.43	0.668	126.9
IC5179	8.193 ± 0.011	0	7.948 ± 0.019	0	3.75 ± 0.012	10	1.477 ± 0.015	10	101.56	0.605	51.9
MCG+12-02-001	9.336 ± 0.011	0	8.84 ± 0.019	0	4.24 ± 0.015	10	1.028 ± 0.012	10	51.24	0.89	173.9
F03359+1523	11.827 ± 0.012	0	11.144 ± 0.022	0	6.563 ± 0.016	10	3.356 ± 0.016	10	20.61	1.0	5.9
NGC1614	8.847 ± 0.011	0	8.378 ± 0.019	0	3.681 ± 0.013	10	0.317 ± 0.026	0	62.29	0.822	163.9
UGC2369	9.762 ± 0.011	0	9.457 ± 0.019	0	5.288 ± 0.017	10	2.163 ± 0.012	10	55.05	0.89	18.5
Arp236	9.223 ± 0.011	0	8.208 ± 0.019	0	4.224 ± 0.012	10	1.159 ± 0.012	10	65.34	0.867	6.9
IC883	10.207 ± 0.011	0	9.639 ± 0.019	0	5.324 ± 0.013	10	2.285 ± 0.012	10	58.29	0.855	178.4
UGC4881	10.379 ± 0.011	0	10.051 ± 0.02	0	6.043 ± 0.013	10	3.255 ± 0.015	10	50.12	0.888	21.9
NGC3690	7.198 ± 0.011	0	6.05 ± 0.019	0	2.227 ± 0.011	10	-1.064 ± 0.011	10	127.09	0.85	21.1
F17132+5313	11.007 ± 0.011	0	10.464 ± 0.019	0	5.886 ± 0.022	10	3.202 ± 0.012	10	31.03	0.916	173.8
MK848	10.775 ± 0.011	0	10.186 ± 0.02	0	5.556 ± 0.013	10	2.123 ± 0.012	10	34.25	0.799	150.5
IRAS10565+2448W	10.772 ± 0.012	0	10.085 ± 0.021	0	5.666 ± 0.014	10	2.388 ± 0.017	10	33.03	1.0	174.8
VII Zw 31	10.735 ± 0.012	0	10.239 ± 0.02	0	5.793 ± 0.018	10	3.163 ± 0.012	10	28.24	1.0	12.6
IRAS23365+3604	11.693 ± 0.012	0	11.026 ± 0.022	0	6.51 ± 0.017	10	2.946 ± 0.012	10	30.84	0.779	20.4

Table 4. Derived *WISE* properties of (U)LIRG Sample

Galaxy	$L_{\text{TIR}}$ ( $\text{Wm}^{-2}$ )	$D_{\text{lum}}$ (Mpc)	$W3_{\text{PAH}}$ (mJy)	$W4_{\text{dust}}$ (mJy)	$W1-W2$ (mag)	$W2-W3$ (mag)	$\log L_{W1}$	$\log L_{W2}$	$\log L_{W3}$	$\log L_{W4}$	$\log L_{W1_{\text{Sun}}}$
Mrk231	12.51 <sup>a</sup>	171.98	1522.2544	7303.187	1.175	3.198	11.3912 ± 0.010	11.4646 ± 0.012	11.5613 ± 0.010	11.9473 ± 0.010	12.7505 ± 0.014
IRAS17208-0014	12.4 <sup>b</sup>	183.01	125.8645	1061.4515	0.84	4.035	10.1566 ± 0.010	10.0962 ± 0.012	10.5327 ± 0.010	11.1637 ± 0.014	11.5159 ± 0.014
Arp220	12.18 <sup>c</sup>	75.99	482.0348	5964.031	0.476	4.53	9.9231 ± 0.010	9.717 ± 0.012	10.3525 ± 0.011	11.1499 ± 0.010	11.2824 ± 0.014
NGC6240	11.86 <sup>d</sup>	104.98	373.4446	2882.1587	0.537	3.576	10.4599 ± 0.010	10.2781 ± 0.012	10.5223 ± 0.012	11.1148 ± 0.010	11.8192 ± 0.014
NGC695	11.7 <sup>d</sup>	139.11	284.3924	679.9062	0.391	4.378	10.3158 ± 0.010	10.0757 ± 0.012	10.6485 ± 0.010	10.732 ± 0.010	11.6751 ± 0.014
Mrk331	11.5 <sup>e</sup>	79.3	345.9611	1839.5452	0.426	4.356	9.9072 ± 0.010	9.6812 ± 0.012	10.2454 ± 0.010	10.6761 ± 0.010	11.2665 ± 0.014
UGC12815	11.42 <sup>d</sup>	61.12	535.5026	1404.9697	0.176	3.609	10.2838 ± 0.010	9.9577 ± 0.012	10.209 ± 0.014	10.3329 ± 0.012	11.6431 ± 0.014
HIPASSJ1004-06	11.37 <sup>e</sup>	79.52	452.5499	1057.5352	0.292	4.304	10.1026 ± 0.010	9.8229 ± 0.012	10.3645 ± 0.014	10.4382 ± 0.011	11.4619 ± 0.014
NGC2388	11.28 <sup>e</sup>	62.09	365.9762	1613.9646	0.341	4.2	9.8183 ± 0.010	9.558 ± 0.012	10.0573 ± 0.011	10.4068 ± 0.010	11.1776 ± 0.014
NGC2146	11.12 <sup>e</sup>	20.56	5237.3984	16063.61	0.343	4.229	10.0006 ± 0.010	9.7413 ± 0.012	10.2528 ± 0.011	10.4446 ± 0.010	11.3599 ± 0.014
NGC1365	11.0 <sup>e</sup>	18.14	3901.5818	11801.377	0.295	3.632	10.0309 ± 0.010	9.7525 ± 0.012	10.0161 ± 0.011	10.2019 ± 0.010	11.3902 ± 0.014
NGC4039	10.88 <sup>f</sup>	21.51	1859.7667	5897.8604	0.169	3.834	9.8258 ± 0.010	9.4971 ± 0.012	9.8426 ± 0.011	10.0488 ± 0.010	11.1851 ± 0.014
UGC89	11.11 <sup>g</sup>	63.89	320.6163	893.426	0.132	3.664	10.0948 ± 0.010	9.7511 ± 0.012	10.0247 ± 0.012	10.1748 ± 0.010	11.4541 ± 0.014
NGC6701	11.11 <sup>g</sup>	60.6	367.7937	1043.429	0.193	4.027	9.9313 ± 0.010	9.6122 ± 0.012	10.0383 ± 0.010	10.1962 ± 0.010	11.2906 ± 0.014
UGC1845	11.13 <sup>g</sup>	66.39	224.3041	746.7936	0.308	3.984	9.7664 ± 0.010	9.493 ± 0.012	9.9029 ± 0.010	10.1303 ± 0.010	11.1257 ± 0.014
NGC5936	11.13 <sup>g</sup>	65.12	361.3966	1041.8303	0.241	4.137	9.9207 ± 0.010	9.6207 ± 0.012	10.0932 ± 0.010	10.2581 ± 0.010	11.2801 ± 0.014
MCG+02-20-003	11.14 <sup>g</sup>	72.42	138.1558	508.2348	1.067	3.527	9.5066 ± 0.010	9.5371 ± 0.012	9.768 ± 0.010	10.0387 ± 0.010	10.8659 ± 0.014
HIPASSJ0716-62	11.16 <sup>g</sup>	47.11	576.0187	1830.9971	0.238	3.76	10.0002 ± 0.010	9.6987 ± 0.012	10.0146 ± 0.011	10.2219 ± 0.010	11.3595 ± 0.014
ESO320-G030	11.16 <sup>g</sup>	40.4	397.64	1557.4791	0.219	3.997	9.6146 ± 0.010	9.3059 ± 0.012	9.72 ± 0.011	10.018 ± 0.010	10.9739 ± 0.014
IC5179	11.22 <sup>g</sup>	49.38	857.0593	2040.4521	0.242	4.2	10.0294 ± 0.010	9.7295 ± 0.012	10.228 ± 0.010	10.3098 ± 0.011	11.3887 ± 0.014
MCG+12-02-001	11.5 <sup>g</sup>	72.07	560.0752	3065.8076	0.52	4.606	9.8937 ± 0.010	9.7051 ± 0.012	10.3716 ± 0.011	10.8149 ± 0.010	11.253 ± 0.014
F03359+1523	11.53 <sup>g</sup>	157.18	66.3665	415.0831	0.719	4.608	9.5629 ± 0.010	9.454 ± 0.012	10.1226 ± 0.011	10.6238 ± 0.011	10.9222 ± 0.014
NGC1614	11.66 <sup>g</sup>	67.1	946.8895	5814.2104	0.474	4.728	10.0285 ± 0.010	9.8215 ± 0.012	10.5376 ± 0.010	11.0308 ± 0.014	11.3879 ± 0.014
UGC2369	11.66 <sup>g</sup>	138.75	199.2178	1247.5616	0.294	4.189	10.2759 ± 0.010	9.997 ± 0.012	10.4916 ± 0.011	10.9934 ± 0.010	11.6352 ± 0.014
Arp236	11.71 <sup>g</sup>	85.76	569.1014	2746.3096	1.044	3.959	10.1017 ± 0.010	10.1226 ± 0.012	10.5296 ± 0.010	10.9181 ± 0.010	11.461 ± 0.014
IC883	11.73 <sup>g</sup>	107.12	201.8004	1022.3195	0.595	4.295	9.8904 ± 0.010	9.732 ± 0.012	10.2725 ± 0.010	10.6822 ± 0.010	11.2497 ± 0.014
UGC4881	11.75 <sup>g</sup>	176.17	98.5039	418.2176	0.321	4.036	10.2297 ± 0.010	9.9615 ± 0.012	10.3932 ± 0.010	10.7262 ± 0.011	11.5891 ± 0.014
NGC3690	11.94 <sup>g</sup>	51.22	3593.5107	21073.629	1.146	3.821	10.4689 ± 0.010	10.5307 ± 0.012	10.8823 ± 0.010	11.3555 ± 0.010	11.8282 ± 0.014
F17132+5313	11.95 <sup>g</sup>	231.0	115.9448	428.5789	0.58	4.574	10.2095 ± 0.010	10.0451 ± 0.012	10.6993 ± 0.012	10.9721 ± 0.010	11.5688 ± 0.014
Mrk848	11.95 <sup>g</sup>	180.69	167.5365	1321.332	0.622	4.667	10.1015 ± 0.010	9.9537 ± 0.012	10.6458 ± 0.010	11.2477 ± 0.010	11.4608 ± 0.014
IRAS10565+2448W	11.99 <sup>g</sup>	188.91	151.349	1045.468	0.725	4.46	10.1385 ± 0.010	10.0318 ± 0.012	10.6404 ± 0.010	11.1847 ± 0.011	11.4978 ± 0.014
VIIZw31	12.0 <sup>g</sup>	230.22	124.3413	458.6414	0.518	4.464	10.307 ± 0.010	10.1178 ± 0.012	10.7267 ± 0.011	10.9986 ± 0.010	11.6663 ± 0.014
IRAS23365+3604	12.19 <sup>g</sup>	269.83	70.1698	676.6337	0.707	4.6	10.0647 ± 0.010	9.951 ± 0.012	10.6162 ± 0.011	11.3054 ± 0.010	11.424 ± 0.014

Table 4 continued





**Table 5.** Measured *WISE* properties of Dwarf Sample

Galaxy	W1 (mag)	W1f (-)	W2 (mag)	W2f -	W3 (mag)	W3f -	W4 (mag)	W4f -	Radius	b/a	P.A.
NGC0625	$8.536 \pm 0.012$	0	$8.46 \pm 0.02$	0	$5.423 \pm 0.033$	10	$2.357 \pm 0.024$	10	227.06	0.406	93.7
NGC1569	$7.484 \pm 0.011$	0	$7.258 \pm 0.019$	0	$3.916 \pm 0.018$	10	$-0.016 \pm 0.011$	10	208.06	0.532	119.9

Table 6. Derived *WISE* properties of Derived Sample

Galaxy	$L_{\text{TIR}}$ ( $\text{Wm}^{-2}$ )	$D_{\text{lum}}$ (Mpc)	$W3_{\text{PAH}}$ (mJy)	$W4_{\text{dust}}$ (mJy)	$W1-W2$ (mag)	$W2-W3$ (mag)	$\log L_{W1}$	$\log L_{W2}$	$\log L_{W3}$	$\log L_{W4}$	$\log L_{W1\text{-Sun}}$
NGC0625	8.50 <sup>a</sup>	4.68	173.3133	870.4055	0.076	3.038	7.8515 ± 0.010	7.4854 ± 0.012	7.4878 ± 0.018	7.8937 ± 0.013	9.2108 ± 0.014
NGC1569	8.57 <sup>a</sup>	1.59	738.7435	7969.3071	0.226	3.342	7.3458 ± 0.010	7.0397 ± 0.012	7.1791 ± 0.013	7.9171 ± 0.010	8.7052 ± 0.014

<sup>a</sup> De Looze et al. (2011)